

# On single-station, six degree-of-freedom observations of local to regional seismicity at the Piñon Flat Observatory in Southern California

Andreas Brotzer  \* <sup>1</sup>, Heiner Igel  <sup>1</sup>, Felix Bernauer  <sup>1</sup>, Joachim Wassermann  <sup>1</sup>, Robert Mellors  <sup>2</sup>, Frank Vernon  <sup>2</sup>

<sup>1</sup>Department of Earth and Environment Sciences, Ludwig-Maximilians-Universität München, Munich, Germany, <sup>2</sup>Institute of Geophysics and Planetary Physics, Scripps Institution of Oceanography, San Diego, USA

**Author contributions:** *Conceptualization:* Andreas Brotzer, Heiner Igel, Frank Vernon. *Methodology:* Andreas Brotzer, Felix Bernauer, Joachim Wassermann. *Formal Analysis:* Andreas Brotzer, Felix Bernauer. *Investigation:* Andreas Brotzer. *Resources:* Heiner Igel, Frank Vernon, Robert Mellors. *Writing - original draft:* Andreas Brotzer. *Writing - Review & Editing:* Andreas Brotzer, Robert Mellors, Frank Vernon, Heiner Igel. *Visualization:* Andreas Brotzer. *Supervision:* Heiner Igel.

**Abstract** In September 2022, a portable, three-component rotational rate sensor, namely a blueSeis-3A gyroscope, was deployed at the underground vault of the Piñon Flat Observatory (PFO) in southern California. A three-component, broadband seismometer is co-located, jointly forming a six degree-of-freedom (DoF) station for long-term observations of local and regional seismicity and multi-component wavefield studies. The seismic recordings are available online via IRIS FDSN services as PY.BSPF (BlueSeis at Piñon Flat).

The instrumentation at PFO additionally provides high-quality strain observations, allowing the study of translation, rotations and strain of the seismic wavefield in a low noise and high seismicity area (e.g. San Andreas fault zone). A seismic array at PFO is used to compute array-derived rotations and validate the direct observations of rotational ground motions. We show results of 6-DoF processing applied to a local  $M_w$  4.1 and a regional  $M_w$  6.2 event to obtain backazimuth estimates, which we validate with array beamforming, and estimates of local seismic phase velocities.

For observed events between October 2022 and October 2023, we detect more than 400 events of which 118 are triggered on all six components. Peak rotation rate amplitudes are used to derive empirical peak amplitude (or magnitude) relations for vertical and horizontal rotation rates to provide valuable insights towards resolvability for comparable 6 DoF campaigns. We find the dominating limitations for rotational motion observations currently to be set by the self-noise level of the blueSeis-3A rotational sensor and encourage further instrumental development.

**Non-technical summary** A portable rotational sensor, called blueSeis-3A, measuring three components of ground rotation has been set up at the Piñon Flat Observatory (PFO) in southern California in 2022. Together with a three component seismometer next to it, six different types of particle motion can be observed at a single station. This enables us to obtain information on seismic wavefields similar to an extended seismic array. For a set of 118 detected events, we show results for different analysis approaches and compare the direct measurement of ground rotation against estimates based on a seismic array at the site. We present a data based relation for rotation rate amplitudes as a function of hypocentral distance and magnitude for local to regional earthquakes. This relation supports future experimental designs towards expected resolvability with a sensor of similar resolution. We conclude that for this first installation of a permanent six degree-of-freedom station in southern California, especially local seismicity is observable. For a sufficient signal-to-noise ratio of seismic events, six degree-of-freedom analysis methods can be successfully applied.

## 1 Introduction

With the emergence of rotational ground motion observations in seismology based on new instrumentation development (e.g. optical fiber or vacuum Sagnac interferometer) at the beginning of this century, a constant drive for improved instrumentation and application in seismology could be observed (e.g., Pancha et al., 2000; Igel et al., 2005; Schreiber et al., 2009). Observations of three-components of rotational ground motions supplement classic observations of three-components

of translational ground motions, thus provide a more complete observation of particle motions considering a full linear elastic seismic wavefield, which is characterized by a total of 12 degrees-of-freedom (3 translation, 3 rotation and 6 independent strain). A co-located broadband seismometer and rotational sensor, with three-components each, are referred to as a six degree-of-freedom (6 DoF) station. 6 DoF observations at a single station enable the application of new processing techniques (e.g., Cochard et al., 2006; Sollberger et al., 2020) to obtain similar information as a seismic array. Beneficial applications comprise, for instance, general

Production Editor:  
Andrea Llenos  
Handling Editor:  
Paula Koelemeijer  
Copy & Layout Editor:  
Sarah Jaye Oliva

Signed reviewer(s):  
Stefanie Donner  
Oliver Lamb

Received:  
July 23, 2024  
Accepted:  
March 19, 2025  
Published:  
May 6, 2025

\*Corresponding author: andreas.brotzer@lmu.de

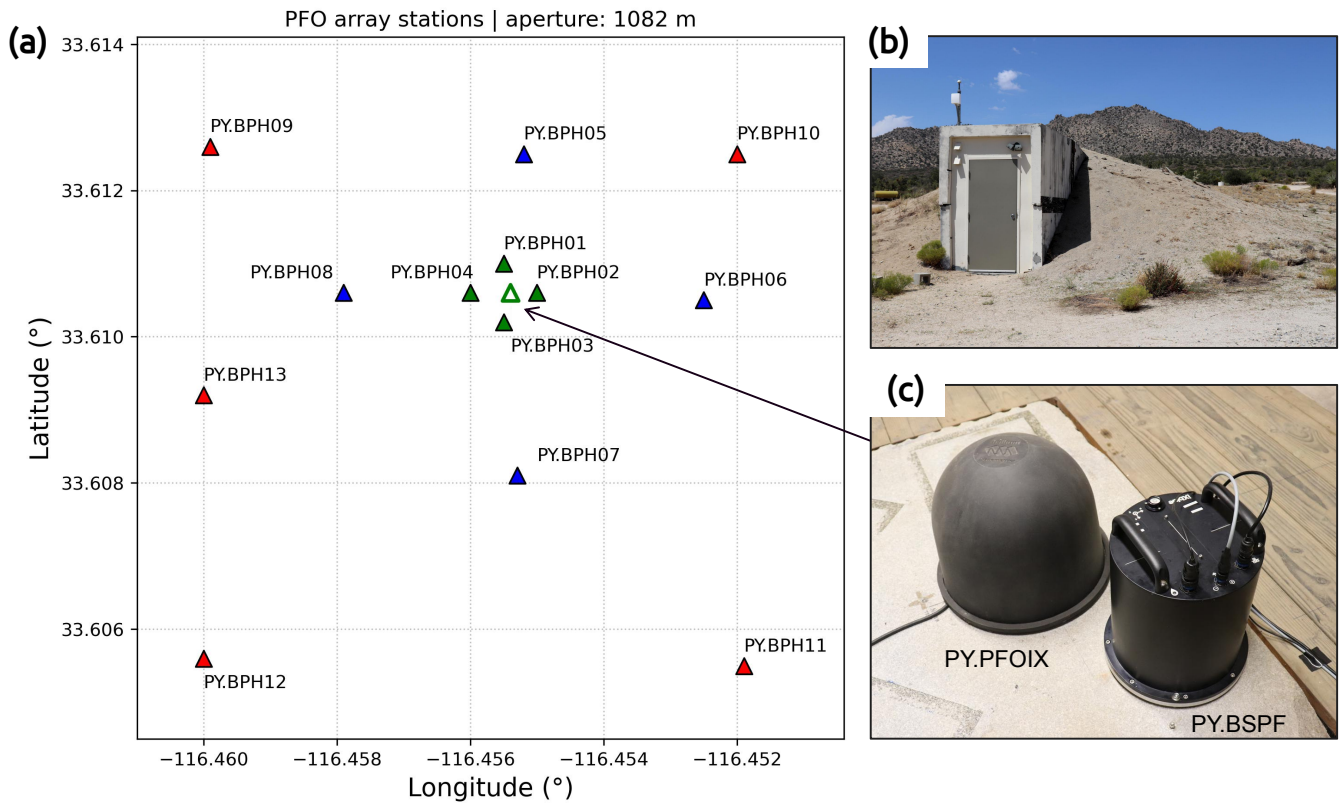


**Figure 1** (a) shows the station map of the seismic array at the Piñon Flat Observatory in southern California. The array is subdivided in an inner array (green stations) and middle array (green and blue stations) and all stations (green, blue and red stations). (b) pictures the entrance of the underground vault, shielding environmental influences, that hosts the (c) 6 degree-of-freedom station (PY.BSPF and PY.PFOIX), including a co-located blueSeis-3A rotational rate sensor and broadband seismometer placed on an isolated granite pillar.

wavefield decomposition by polarization analysis (Sollberger et al., 2018, 2020), near-surface site characterization (Keil et al., 2021; Singh et al., 2020), improved structural health monitoring (e.g., Zembaty et al., 2016; Trifunac, 2009; Bońkowski et al., 2023; Guéguen et al., 2020; Guéguen and Astorga, 2021), enhanced moment tensor inversion (Donner et al., 2016, 2018, 2020; Donner, 2021; Ichinose et al., 2021) and dynamic tilt correction of horizontal components of seismometers (Bernauer et al., 2020; Lin et al., 2022), especially for ocean-bottom seismometers (e.g., Lindner et al., 2016), source tracking (Yuan et al., 2020; Chen et al., 2023), teleseismic observations (e.g., Igel et al., 2005; Schmelzbach et al., 2018; Abreu et al., 2023) or for applied exploration data analysis (e.g., Schmelzbach et al., 2018). An increased information gain for single-station observations holds potential for studies on extraterrestrial bodies (Bernauer et al., 2020). Currently, a variety of rotational sensors are operated and developed, such as large-scale ring lasers (Igel et al., 2021; Belfi et al., 2017), fiber-optical gyroscopes (e.g., Bernauer et al., 2018), mechanical beam balances (e.g., Venkateswara et al., 2017; McCann et al., 2021; Ross et al., 2017a, 2023) or fluid based sensors (e.g., Bernauer et al., 2012). However, to fully exploit the above-mentioned variety of benefits for seismological applications, portable rotational sensors with improved sensitivity across a wide frequency range are required. Brotzer et al. (2023) characterized the rotational background noise level to set a benchmark for instrumenta-

tion development.

Until recently, wavefield gradients, in particular rotations, were commonly neglected in seismological analysis and modelling due to their small amplitudes (Aki and Richards, 2002) and a lack of instrumentation to observe the rotational motion of the seismic wavefield. While direct observations of local surface strain are observed for decades (e.g., Agnew and Wyatt, 2003), it was a challenge to observe weak rotational ground motions (e.g., Schreiber et al., 2014). Technical advances in recent years, in particular optical sensing and read-out technologies, resulted in new instrumentation (Bernauer et al., 2012, 2021) to directly access rotational ground motions (e.g. fiber-optical gyroscopes, beam balance rotational sensors) and dynamic ground strain (e.g. distributed acoustic sensing). This also called for the ongoing development of open-source packages for 6 DoF signal analysis, such as TwistPy (Sollberger, 2023; Sollberger et al., 2023). Most experiments employing portable rotational sensors for 6 DoF observations and processing were short-term field deployments for specific case studies (e.g., Wassermann et al., 2020; Yuan et al., 2020; Sbaa et al., 2017; Perron et al., 2018; Takeo, 2009; Eibl et al., 2022). A one-component, horizontal ring laser gyroscope, called GEOsensor, was installed at Piñon Flat Observatory (PFO) in 2005 (Schreiber et al., 2009) and dismantled in 2022. We report on a long-term deployment of a three-component blueSeis-3A rotational sensor (Bernauer et al., 2018) next to a three-

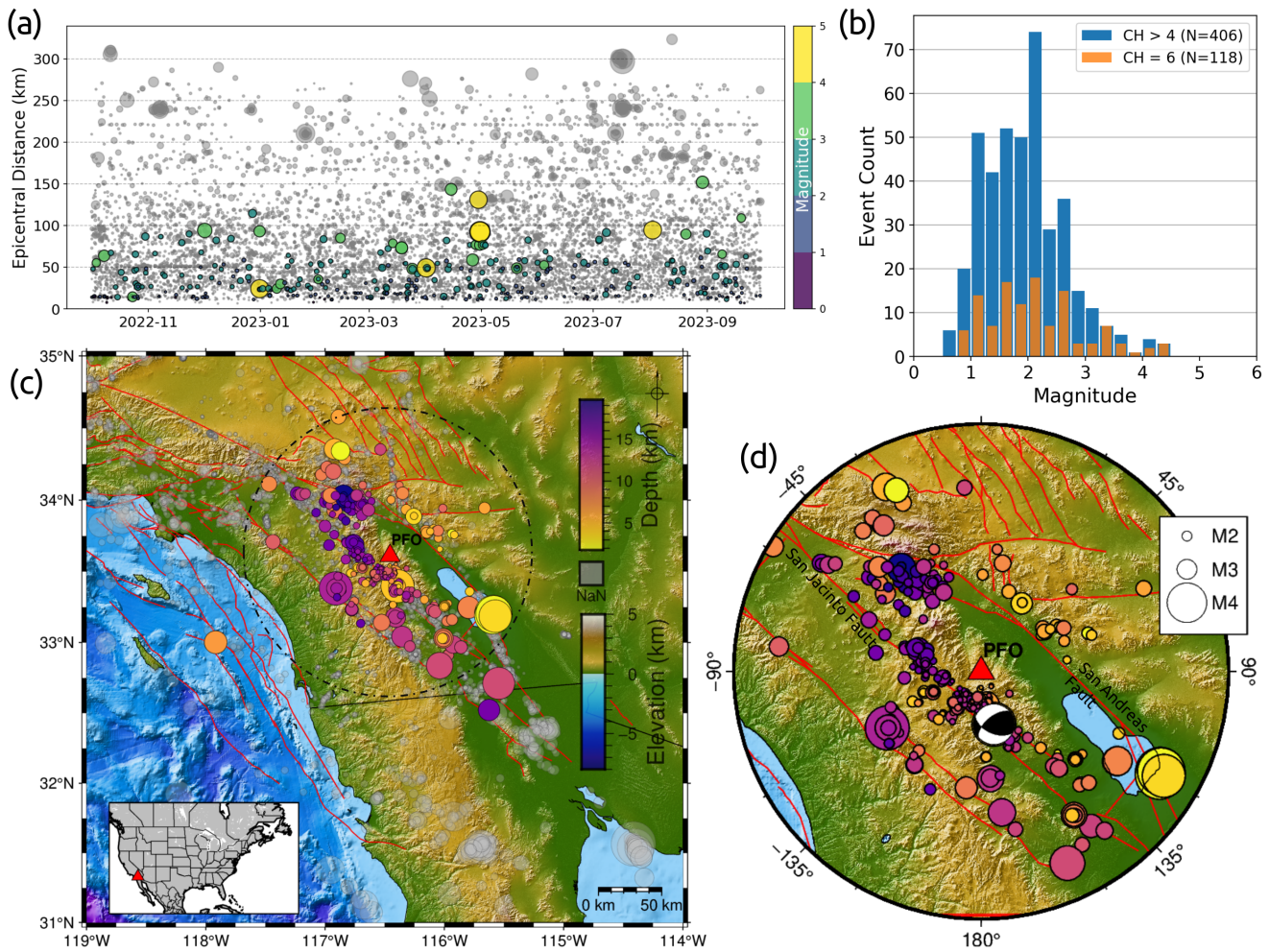


**Figure 2** The regional seismicity around the Piñon Flat Observatory (PFO) in southern California based on the USGS catalog from October 2022 to October 2023 is shown over time (a) and as geographic distribution (c), including known fault lines (Dataset., 2013) as red lines. Events are scaled by magnitude and detected events (coincidence  $\geq 4$ ) on the six degree-of-freedom station are color-coded by magnitude (a) and by depth (b-c). A histogram by magnitude of the total count of 406 detected events (b) on at least 4 of 6 channels (blue) are compared to 118 events detected on all 6 channels (orange). A focus on the local area around PFO (d) displays triggered, local events and a centroid moment tensor of the  $M_w$  4.1 event (2022-12-31 12:12:26 UTC) at an epicentral distance of 24.3 km from PFO.

component, broadband seismometer forming a 6 DoF station at PFO in southern California as replacement for the GEOsensor. The PFO is located between the San Andreas (25 km NE) and the San Jacinto fault zone (14 km SW) systems (Agnew and Wyatt, 2003), which are seismically active fault zones on the Southern California segment of the Pacific and North-American plate boundary. The 6 DoF data is openly accessible online and provides an opportunity to apply 6 DoF analysis to local and regional seismicity.

## 2 Deployment

Currently, most 6 DoF stations are deployed for short-term field measurements (e.g., Wassermann et al., 2020; Sbaa et al., 2017; Yuan et al., 2020; Eibl et al., 2022). In late September 2022, a first permanent (= open-end) 6 DoF station was installed on an isolated granite pier inside the underground test facility (= vault) at the Piñon Flat Observatory (PFO) in Southern Califor-

nia (see Fig. 1). The depth of the sensor below the surface is about 6 m, while the granite pier extends another 1.5 m downwards. Hence, the installation benefits from good coupling to the sub-surface while being decoupled from the vault, as well as stable ambient temperature conditions. The station consists of a portable, fibre-optic gyroscope blueSeis-3A sensor (by Exail, formerly iXblue), measuring three-components of rotational ground velocity (rad/s). This rotational sensor is provided by the Incorporated Research Institutions for Seismology (IRIS), now EarthScope Consortium. A full characterization of the blueSeis-3A was conducted by Bernauer et al. (2018). The data are openly accessible via IRIS FDSN service (UC San Diego, 2014) with seed code: PY.BSPF..HJ\* (with 200 Hz). All metadata is specified in a stationXML.

A Trillium T120 broadband seismometer (by Nanometrics) provides three-components of translational ground motion observations (II.PFO.10.BH\* with 40 Hz). Since April 02, 2023, a STS-2 seismometer (by

Streckeisen), named PY.PFOIX..HH\*, was installed next to the blueSeis-3A, in order to provide translation and rotation observations up to about 50 Hz (based on a sampling rate of 200 Hz and the transfer function of the STS-2). The complete 6 DoF station (= six components) is hereafter referred to as BSPF. The seismic array stations (PY.BPH\*.BH\* with 40 Hz) is a mix of Trillium 120s (by Nanometrics) and STS-5A (by Streckeisen) sensors (UC San Diego, 2014).

### 3 Dataset

Generally, a basic, yet rapid event analysis is provided to the scientific community by an integration of the BSPF station into the rotational event database (Salvermoser et al., 2017). In this study, we analyze one year of data from October 01, 2022 until September 30, 2023. Figure 2 shows all events listed by the USGS catalog in the given time period and the geographic boundaries shown in Figure 2c (gray and colored circles). Most of the local seismicity is occurring along the nearby northwest-southeast oriented fault systems (red lines), including the San Jacinto fault and the San Andreas fault system (Fig. 2d). A prominent cluster of local seismicity is located to the south of PFO, referred to as the Trifurcation seismicity cluster (Ross et al., 2017b).

#### 3.1 BSPF: Direct Rotations

We use a recursive STA-LTA coincidence trigger of the ObsPy package (Beyreuther et al., 2010) to detect seismic events recorded on at least four of the six channels of BSPF. The STA window is 1.5 s and the LTA window is 10 s with an upper and lower threshold of 2 and 1.2, respectively. This allows a distinction between events with coincidence of 4, 5 and 6 depending on the amount of triggered channels. This generally includes three translational channels, due to the enhanced signal-to-noise characteristics of the broadband seismometer, plus N channels of the rotational sensor. The event count by magnitude shown in Figure 2b reveals that only 118 events are detected with a coincidence of 6 out of 406 events with a coincidence of at least 4. Triggered events are color-coded by magnitude in Figure 2a, and by depth in 2c and 2d. The seismicity detected by the 6 DoF station is limited to local seismicity within a radius of about 150 km around PFO (Figs. 2a and 2d). An exception is the  $M_w$  6.2 regional event on 2022-11-22, with an epicentral distance of about 312 km (Fig. 5). Triggered event times are matched to events in the USGS catalog via a nearest-time criteria.

Figure 3 displays a selection of detected events with a coincidence of 6 as recorded with BSPF. The recordings of the co-located broadband seismometer are presented in the supplementary Figure S1. The magnitudes range from 1.1 to 3.6, while epicentral distances range from 11 km to 115 km. Peak ground rotation velocities (PGRV) range from  $0.6 \mu\text{rad/s}$  to  $16.4 \mu\text{rad/s}$ . A strong variation of signal-to-noise ratio (SNR) can not only be observed across events, but also across different components. For the entire dataset, the SNR for PY.BSPF does not exceed 10, while for most events an SNR of about

2 is found. This is a result of the still relatively high instrumental self-noise level of the blueSeis-3A sensor (Bernauer et al., 2018).

#### 3.2 Array-Derived Rotations

We use the seismic array at PFO to derive rotational ground motions, serving as a reference for our single-point, direct measurements. Commonly, three-component ground velocities observations are used in a finite-difference approach to estimate three-components of ground rotation across the area of the array (e.g., Spudich and Fletcher, 2008; Poppeliers and Evans, 2015). We employ an implementation for array-derived rotation (ADR) computations in the ObsPy package (Beyreuther et al., 2010). Although these derived-rotations are a good estimate (Suryanto et al., 2006) for frequency bands imposed by the geometry of the seismic array (e.g., Poppeliers and Evans, 2015; Donner et al., 2017), assumptions, such as a rigid plate across the seismic array, result in uncertainties with regard to true ground rotations. Nevertheless, ADR can still be used for validation as it represents an independent measurement within the given assumptions.

The seismic stations at PFO are shown in Figure 1a. We subdivide the seismic array into three subarrays, thus frequency ranges, to compute ADR. The frequency limits for ADR computation as described by Donner et al. (2017) requires an apparent velocity and the aperture of the array (Tab. 1). For the analysis, the frequency bands were conservatively adjusted to a narrower range ( $f_{min}$ - $f_{max}$  in Tab. 1) for the comparison. The inner array (green stations in Fig. 1) comprises five seismic stations and provides the highest frequency band from 1 Hz to 5 Hz (*i*ADR). By extending the *inner* array by four more seismic stations (blue stations in Fig. 1), we define a *mid* array to compute ADR for a frequency band from 0.5 Hz to 1 Hz (*m*ADR). Finally, by including all 14 seismic stations for *all* array provides ADR between 0.1 Hz and 0.5 Hz (*a*ADR).

Some stations of the seismic array at PFO had to undergo maintenance for certain time periods, hence could not be used for ADR computations for events within these periods. The station PY.BPH05 was down for the whole year of interest, unfortunately.

#### 3.3 Signal-to-Noise Ratio

The SNR is a good measure for signal quality. We computed SNRs automatically for each triggered event for direct rotation rate, array-derived rotation rate and acceleration as well as each frequency band (see Tab. 1). The SNR is defined as the maximum of absolute amplitudes in a 15 second window following the trigger time. The noise level is computed as the maximum of absolute amplitudes of a 15 second window of data before the trigger time, being shifted 2 seconds back in time in order to avoid event signals.

Figure 4 provides a statistical analysis of the signal-to-noise ratios and shows histograms for signal-to-noise estimates for all three components of ADR, direct rotation observations of BSPF and translation motion for all

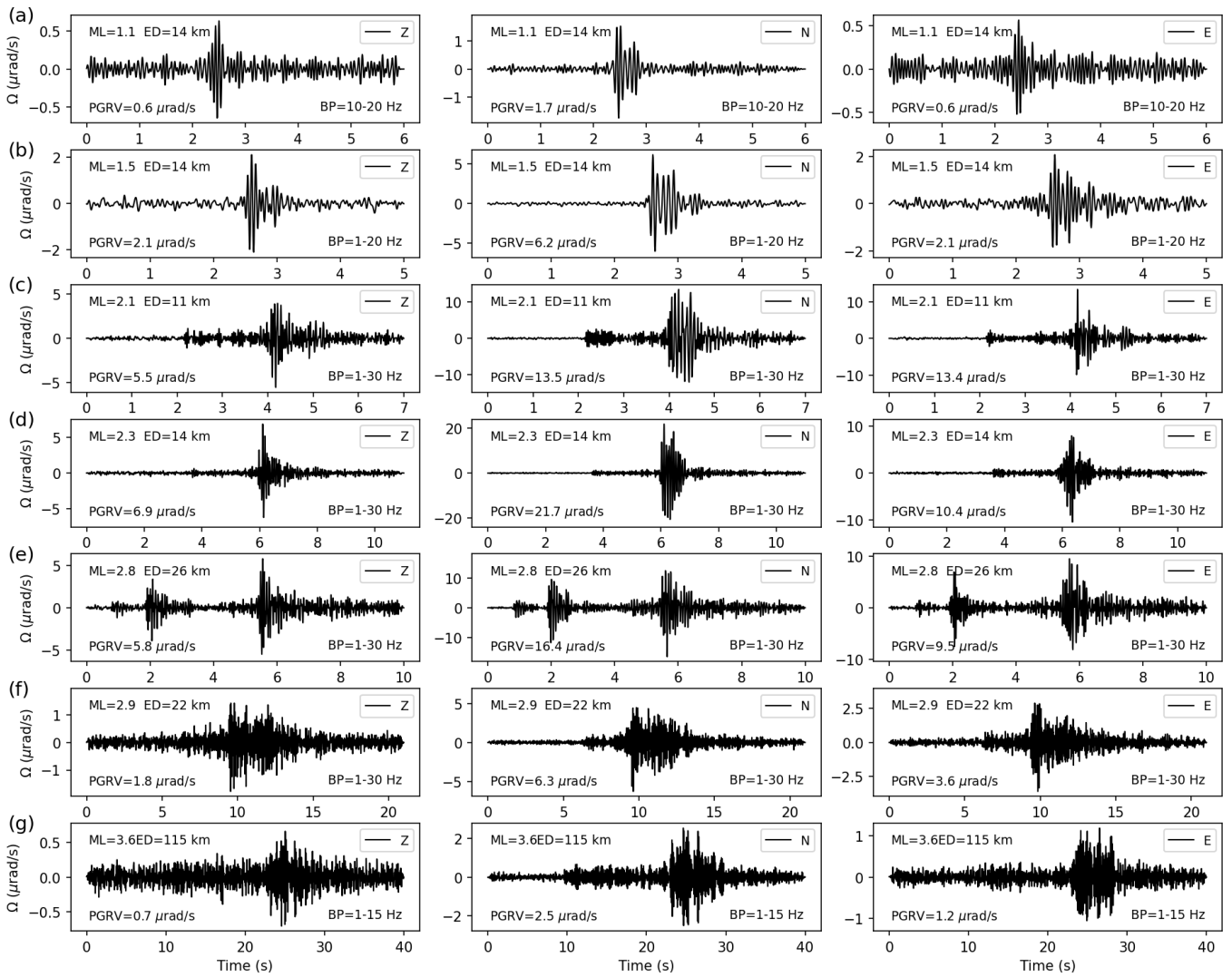


**Figure 3** (a) to (g) show a selection of events detected by BSPF across magnitudes ( $1.1 < M < 3.6$ ) and epicentral distances ( $11 \text{ km} < ED < 115 \text{ km}$ ). Each column displays one component of rotational rate observation (Z, N, E from left to right). Peak ground rotation velocity (PGRV) and the applied bandpass filter (BP) is shown for each record. The origin times are found in Tab. 2. The recording in (e) comprises two events.

subarray	code	# stations	aperture (m)	$f_{min}$ (Hz)	$f_{max}$ (Hz)	f1 (Hz)	f2 (Hz)
all stations	aADR	14	1082	0.1	0.5	0.01	0.7
mid stations	mADR	9	501	0.5	1.0	0.01	1.5
inner stations	iADR	5	93	1.0	5.0	0.08	8.1

**Table 1** Parameters used to subdivide the seismic array at Piñon Flat Observatory (PY.BHP) to three subarrays (see Fig. 1) to compute array-derived rotations for different frequency bands ( $f_1$ - $f_2$ ), based on Donner et al. (2017), imposed by the subarray aperture and apparent velocity of 3000 m/s. For the analysis, the frequency bands were conservatively adjusted to a narrower range ( $f_{min}$ - $f_{max}$ ).

Panel	Start time (UTC)	Magnitude	Type	Depth (km)	ED (km)	BAz (°)	Region
(a)	2022-10-01T05:36:14	1.1	ML	9	14.3	199.7	Anza, CA
(b)	2022-10-02T03:25:19	1.5	ML	8	14.9	199.4	Anza, CA
(c)	2023-09-11T09:20:16	2.1	ML	9	11.6	188.1	Anza, CA
(d)	2023-03-01T22:49:03	2.3	ML	11	14.0	188.7	Anza, CA
(e)	2022-10-26T08:14:38	2.8	ML	14	26.8	276.5	Anza, CA
(f)	2024-02-27T22:50:48	2.9	ML	13	22.9	161.8	Borrego Springs, CA
(g)	2024-02-16T07:38:50	3.6	ML	13	115.7	294.5	Ontario, CA

**Table 2** Detailed information on earthquakes shown in Figure 3. ED = epicentral distance; BAZ = theoretical backazimuth.

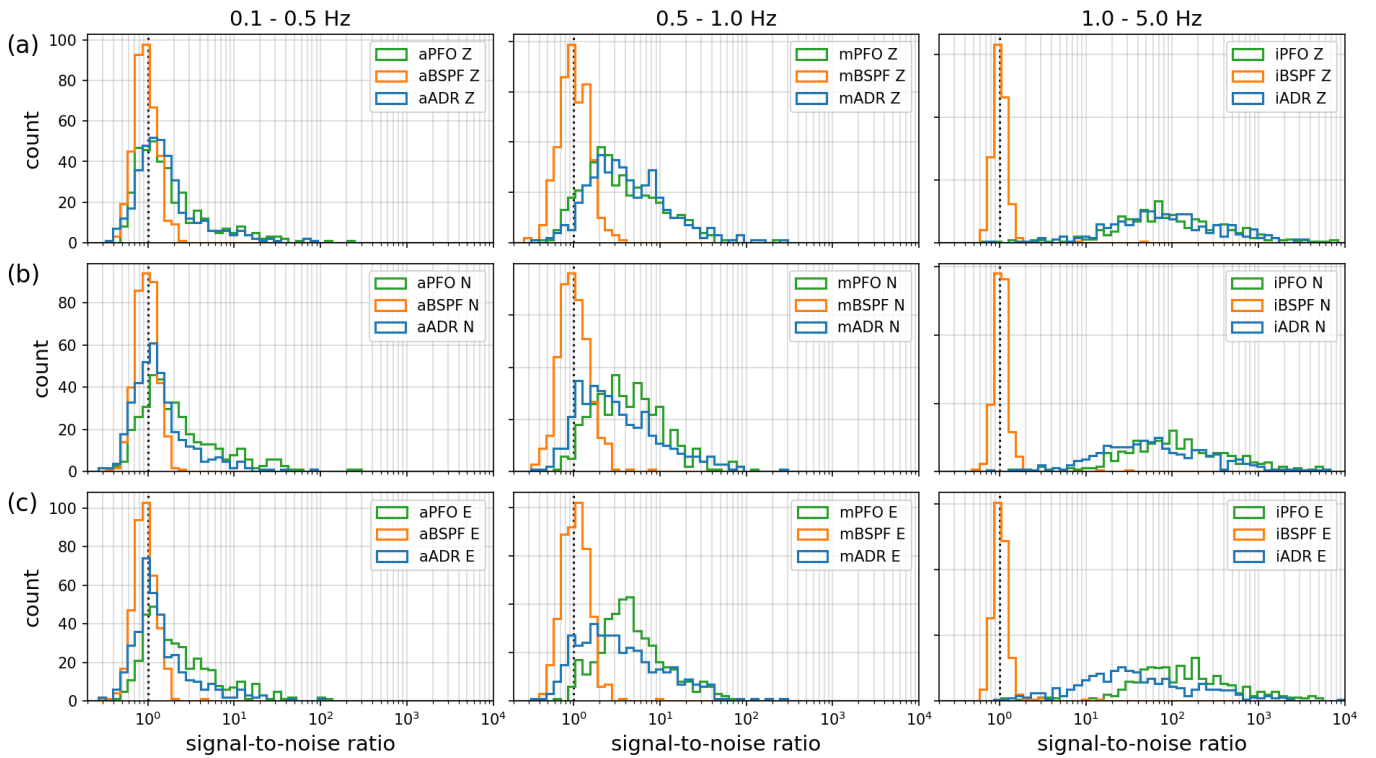


**Figure 4** The panels show histograms of signal-to-noise ratios computed for 398 events for acceleration (PY.PFO), array-derived rotation rate (ADR) and direct rotation rate (PY.BSPF) by component Z, N and E from top to bottom and by frequency band *a* (0.1-0.5 Hz), *m* (0.5-1.0 Hz) and *i* (1.0-5.0 Hz) from left to right.

three frequency bands ( $a = 0.1\text{-}0.5$  Hz,  $m = 0.5\text{-}1.0$  Hz,  $i = 1.0\text{-}5.0$  Hz), corresponding to the subarrays used for ADR computation. For local seismicity, commonly a higher signal content for higher frequencies is expected and observed. Therefore, an increase in signal-to-noise ratio is observed for seismometer data (PFO) for the frequency band *m* ( $\text{SNR} \approx 2\text{-}3$ ) and *i* ( $\text{SNR} \approx 80\text{-}100$ ) compared to band *a*, where noise dominates ( $\text{SNR} \approx 1$ ). This tendency can be seen across all components. Since ADR benefits from the low-self noise of the seismometer, the behavior is equivalent. For direct rotation rate observations of BSPF the SNR is close to 1, while it improves for band *i* with higher frequencies. However, most signal energy for rotational ground motion is found well above 5 Hz and is not reflected in this analysis focusing on frequency bands comparable with ADR. Most detections are based on high peak rotation rates, which are found, especially for local and small magnitude events, at frequencies above 5 Hz. Based on the poor signal-to-noise ratio for most events, the following analysis focuses on two exemplary events with good quality waveforms.

## 4 6 DoF Analysis

Hereafter, we show results of an exemplary 6 DoF analysis for two selected events, a regional  $M_w$  6.2 and a local  $M_w$  4.1.

### 4.1 Event M6.2

The  $M_w$  6.2 event occurred on 2022-11-22 (16:39:05 UTC) in Baja California about 312 km south of PFO (outside the boundaries of Figure 2c) and was recorded with the

6 DoF station. This event represents the largest magnitude recorded up to now and provides energy in the lower frequency *a*-band (0.1-0.5 Hz, see supplementary Figure S2), thus enabling a comparison with ADR for lower frequencies. However, at this time, there is no data available for station BPH02, BPH03 and BPH05, in turn affecting the array-derived rotation rate estimates, in particular the north-south component.

Waveforms of array-derived rotation rate observations and direct rotation rate observations for this event are compared in Fig. 5 across all three frequency bands defined in Tab. 1. Zero-lag cross-correlation (CC) values are as high as 0.97 for the east component (0.5-1.0 Hz). The correlation of the north component is reduced to 0.83, most likely due to missing station data for ADR computations. For the inner array two stations are missing, which affects the ADR computation and results in a poor waveform match (Fig. 5) as well as analysis results.

### 4.2 Event M4.1

On December 31, 2022, a  $M_w$  4.1 event occurred southeast of PFO at an epicentral distance of 24.3 km. Waveforms of this event were recorded with the 6 DoF station and compared to ADR estimates in Figure 6. For ADR computations at this time, station PY.BPH05 (Fig. 1a) is missing, having an influence on the north-south geometry of ADR visible in the waveform comparison in Figure 6. This is quantified by lower ADR amplitudes of the north-component and smaller CC coefficients in Figure 6. Zero-lag CC coefficients between ADR and direct rotation rates are above 0.87 and as high as 0.96 for the east component of the *m*-band. For this fre-

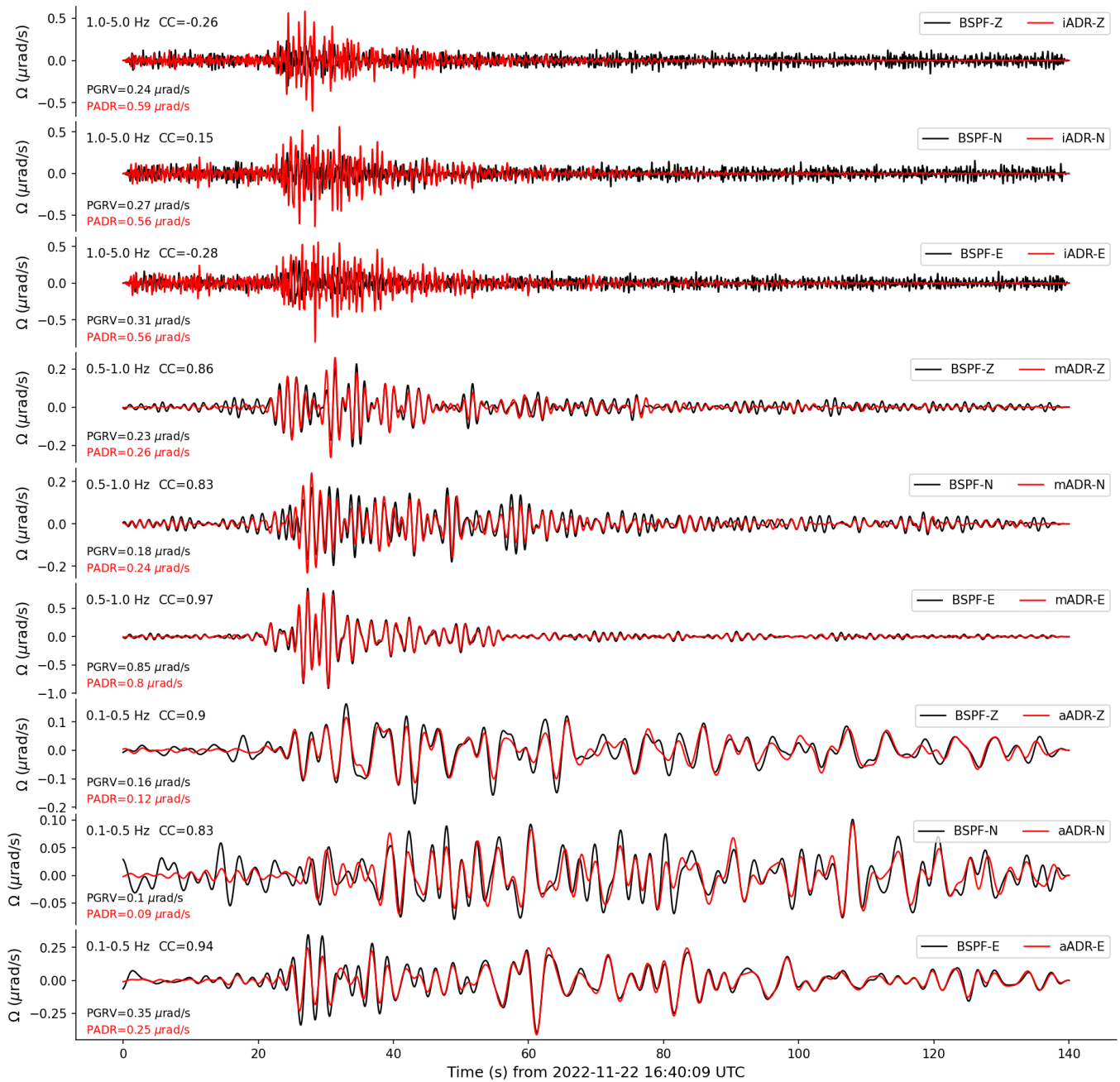


**Figure 5** Direct (black) and array-derived rotational rate (ADR) waveforms of the  $M_w$  6.2 event (2022-11-22 16:39:05 UTC) at an epicentral distance of 312 km are shown. Top to bottom all three components (Z, N, E) are compared in three different frequency bands (top to bottom: 1.0-5.0 Hz, 0.5-1.0 Hz, 0.1-0.5 Hz) according to the PFO inner subarray (*iADR*), mid subarray (*mADR*) and the entire array (*aADR*). An almost perfect phase and amplitude fit of array-derived and direct rotation rate is observable for the east component in the mid-frequency array with a cross-correlation (CC) coefficient of 0.97. (Self-) noise dominates the PY.BSPF recording for the low frequencies (0.1-0.5 Hz). Especially for the north component of the high frequency range (1.0-5.0 Hz), the effect of missing station data for ADR computation is recognizable.

quency band, signal amplitudes are in good agreement, although ADR seems to slightly underestimate peak amplitudes. For frequencies within 1 Hz to 5 Hz, the phase match between *iADR* and BSPF results in CC values of up to 0.9 (east component), while peak amplitudes differ significantly. *iADR* underestimates peak rotations by 47% (Z), 73% (N), 42% (E). ADR generally reveals smaller amplitudes than direct measurements, hence underestimating single-point, rotational ground motion observations. ADR is an estimate dependent on the array geometry, amplitude calibration of the sensors and

assuming a rigid, homogenous plate below the array, thus averaging over local heterogeneities (Spudich and Fletcher, 2009b). This may contribute to differences of a single-station observation. The main frequency content for the local  $M_w$  4.1 is above 5 Hz for the rotation rates observed by PY.BSPF (Figure 7). For the *a*-band, the SNR is poor and the waveforms are dominated by instrumental self-noise, thus not suitable for interpretation (see Fig. 6).

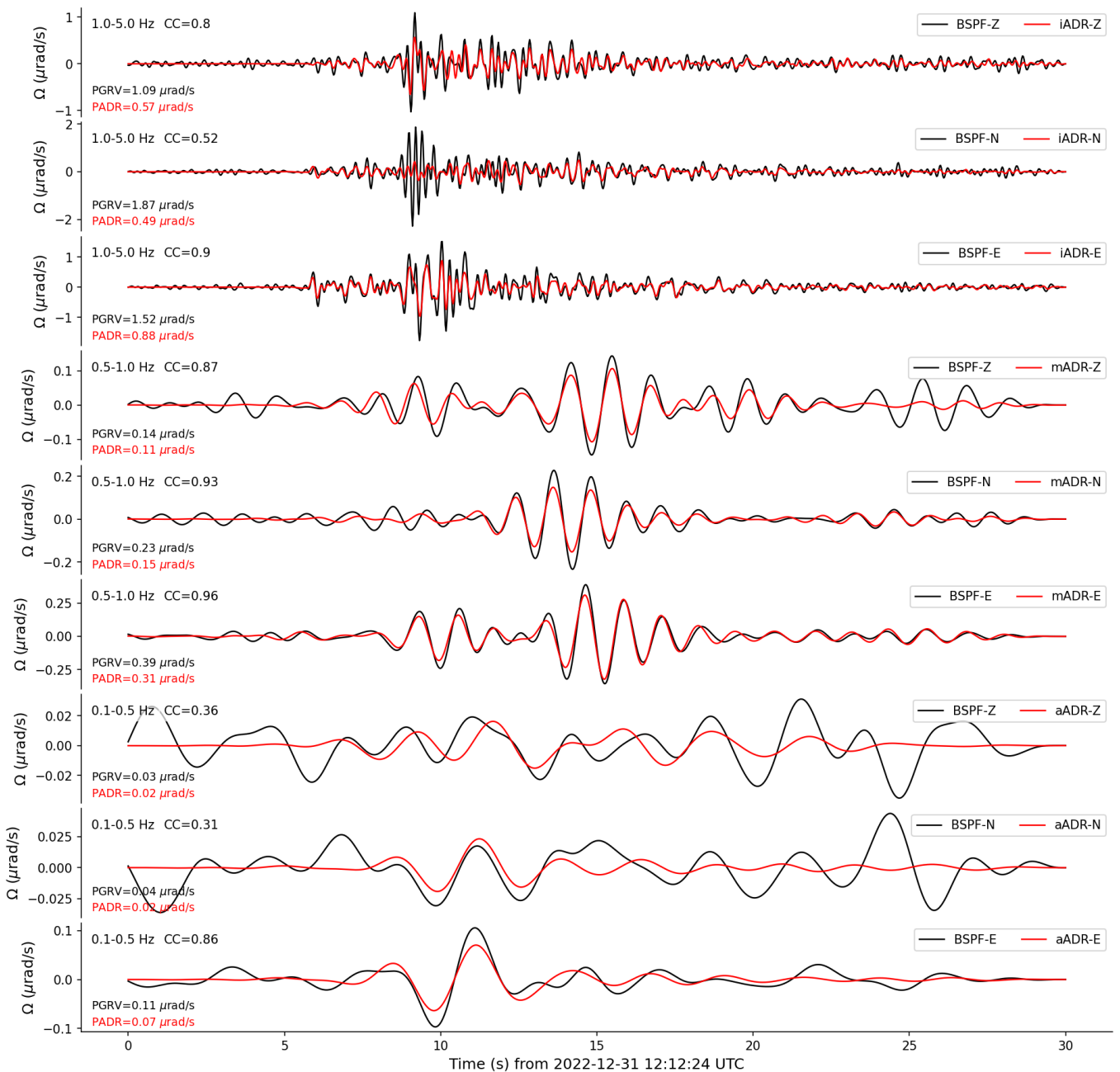


**Figure 6** Direct (black) and array-derived rotational rate (ADR) waveforms of the  $M_w$  4.1 event (2022-12-31 12:12:26 UTC) at an epicentral distance of 24.3 km are shown. Top to bottom all three components (Z, N, E) are compared in three different frequency bands (1.0-5.0 Hz, 0.5-1.0 Hz, 0.1-0.5 Hz) according to the PFO inner subarray (*iADR*), mid subarray (*mADR*) and the entire array (*aADR*). An almost perfect phase and amplitude fit of ADR and direct rotation rate is observable for the mid-frequency band with a cross-correlation (CC) coefficient up to 0.96 (east component). Instrumental self-noise dominates the PY.BSPF recording for frequencies between 0.1-0.5 Hz. In particular, for the north component of the high frequency range (1.0-5.0 Hz), the effect of missing station data for ADR computation is recognizable.

### 4.3 Backazimuth Estimation

With a single 6 DoF station, observing co-located acceleration and rotation rate, the backazimuth of a plane wave can be estimated by exploiting the polarization information of particle motion (e.g., Igel et al., 2007, 2014; Sollberger et al., 2020). The following approaches are compared:

1. *Love polarization*: A grid search across the backazimuth range used to rotate horizontal acceleration to transverse acceleration, which is correlated

with vertical rotation rate. This is a Love wave polarization filter and is applied for overlapping time windows along the event. A zero-lag CC value is computed for all backazimuths for each time window. The maximum of all CC values then provides a backazimuth estimate.

2. *Rayleigh polarization*: A grid search across the backazimuth range used to rotate horizontal rotation rate to obtain transverse rotation rate, which is correlated with vertical acceleration. This is a Rayleigh wave polarization filter. The backazimuth

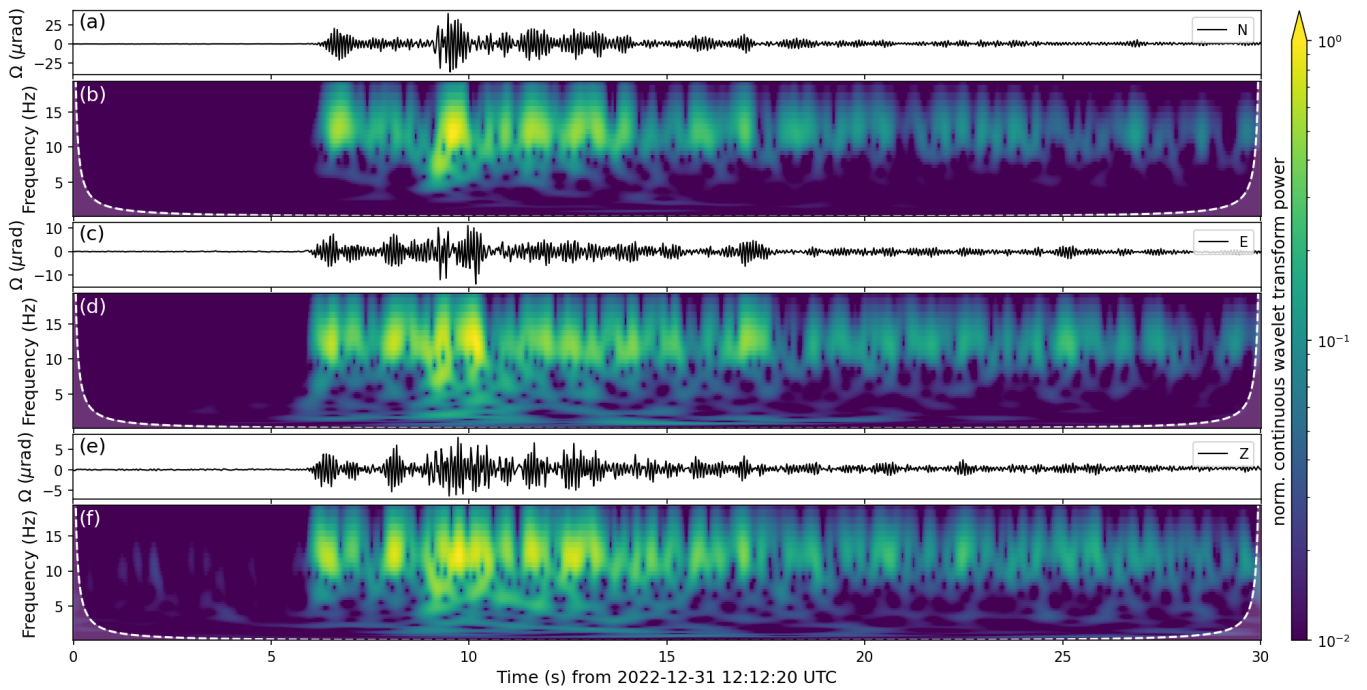


**Figure 7** (a), (c) and (e) show rotation rate records of the  $M_w$  4.1 event (2022-12-31 12:12:26 UTC) for north, east and vertical component, respectively, while (b), (d) and (f) show corresponding spectrograms based on the continuous wavelet transform.

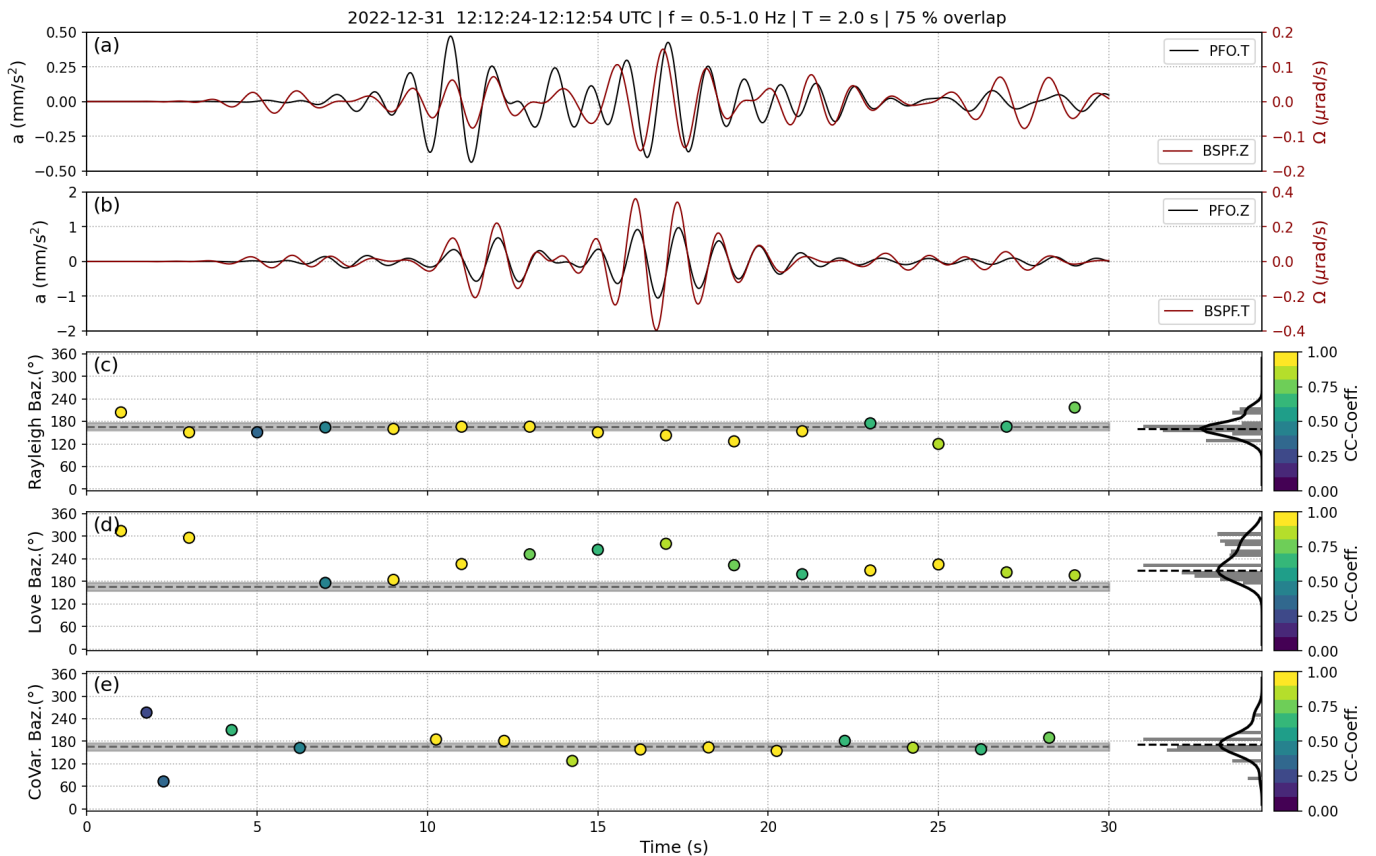


**Figure 8** Comparison of backazimuth estimates for the  $M_w$  4.1 event (2022-12-31 12:12:24 UTC) event. Waveforms are shown for (a) transverse acceleration (black) and vertical rotation rate (red) (= Love waves) as well as (b) vertical acceleration (black) and transverse rotation rate (red) (= Rayleigh waves), using the expected backazimuth to obtain transverse components. Polarization-based grid search for backazimuth estimates using (c) Rayleigh waves and (d) Love waves. (e) covariance optimization of horizontal rotation rate with polarization filter using vertical acceleration. All backazimuth estimates are computed in 2 s time windows with 75% overlap. (c) to (e) shows a histogram, weighted by cross-correlation (CC) coefficient, and a probability density function with the picked maximum (dashed line) is shown on the right y-axis. The expected backazimuth, based on the catalog epicenter location, at  $166^\circ$  is shown as a black, dashed line with a  $\pm 10^\circ$  interval in gray.

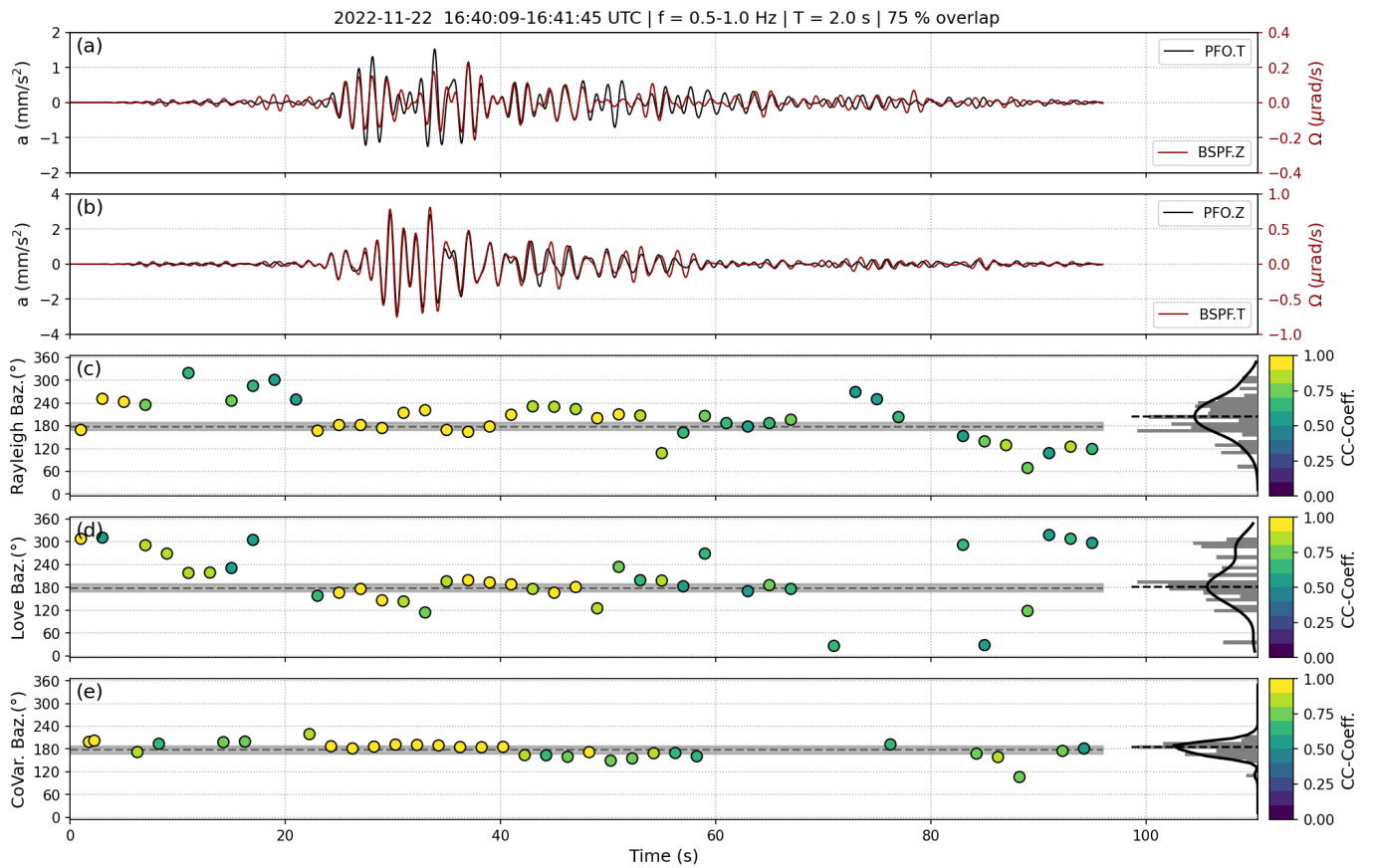


**Figure 9** Comparison of backazimuth estimates for the  $M_w$  6.2 event (2022-11-22 16:39:05 UTC). (a) Waveforms for transverse acceleration (black) and vertical rotation rate (red). (b) Waveforms for vertical acceleration (black) and transverse rotation rate (red). Backazimuth estimates for moving time windows for the (c) grid search based approach using Rayleigh polarization, (d) grid search based approach using Love polarization and (e) using covariance optimization of horizontal rotation rate observations with polarization information of vertical acceleration. All estimates are color-coded by the zero-lag cross-correlation (CC) coefficients. For all backazimuth estimates, a histogram, weighted by CC coefficient, and a probability density function with its maximum is shown on the right y-axis (c-e). The expected backazimuth, based on the catalog epicenter location, at 179 degree is shown as a black dashed line with a  $\pm 10^\circ$  interval in gray (c-e).

estimate is determined as described for the Love polarization above.

3. *Covariance (CoVar) approach*: Based on a classic three component single-station approach using both horizontal components, hence dominantly Rayleigh waves. An estimate of the backazimuth angle is obtained by determining the first eigenvector of the covariance matrix based on the north and east component of rotation rate. The angle is obtained computing the tangent of north over east. A remaining 180 degree ambiguity can be resolved by evaluating the sign of the CC value between vertical acceleration and transverse rotation rate, which should be in phase.

The window length is set to 2 seconds with 90% overlap. Each backazimuth estimate is color-coded by the respective zero-lag, CC value. An overall backazimuth estimate is obtained by using the peak of a kernel-density estimate using Gaussian kernels of the correlation-weighted distribution (e.g., Fig. 8). A minimum CC value of 0.2 is required for a backazimuth estimate to be considered for the kernel-density estimate. With an expected backazimuth of 166 degrees and

179 degrees for the two events, the seismic waveform for both analyzed events arrives from the south and most horizontal rotation caused by Rayleigh waves will be present on the east component, while hardly any rotational motion around the north component is expected. The seismic energy present on the north component might result from scattered phases arriving from different backazimuths and local strain-to-rotation coupling caused by local heterogeneities. Figure 8 and Figure 9 show backazimuth estimates for all three approaches listed above, each compared to the expected backazimuth based on the catalog event location for the  $M_w$  4.1 event and  $M_w$  6.2 event, respectively. Waveforms are bandpass filtered between 0.5 Hz to 1.0 Hz and are shown for different combinations of acceleration and rotation rate using the expected backazimuth for matrix rotation (Fig. 8a-c and Fig. 9a-c). Due to the proximity of the source location for the  $M_w$  4.1 event, there is no clear phase separation, nonetheless, a decent waveform fit is observed (Fig. 8). The backazimuth estimates for Rayleigh waves and the CoVar approach yield directions close to the expected backazimuth with CC values above 0.9, while for Love wave estimates the CC values are reduced and the directions differ signifi-

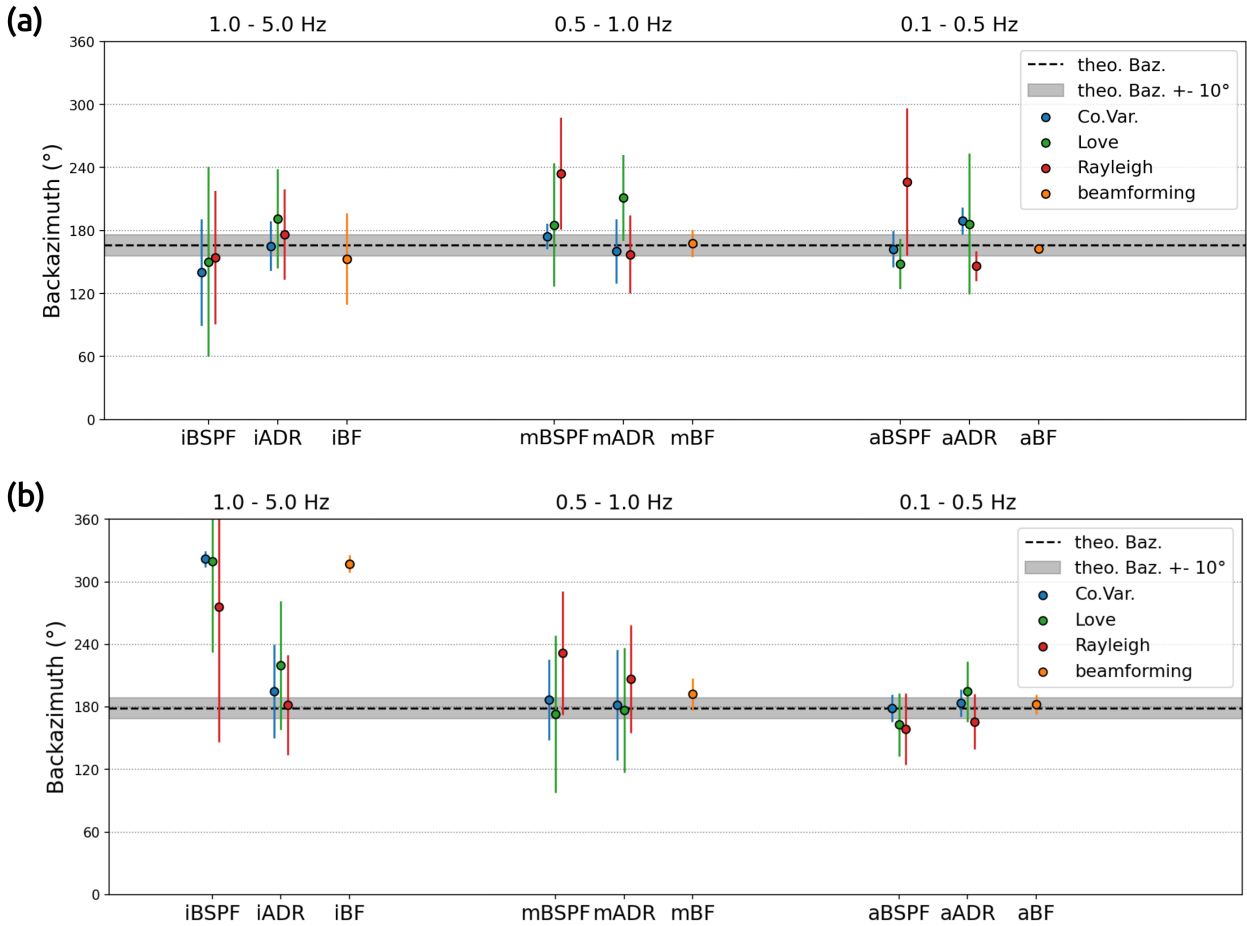


**Figure 10** Comparison of backazimuth estimates for (a) the  $M_w$  4.1 event and (b) the  $M_w$  6.2 event. Shown mean estimates and their standard deviation are based on Gaussian kernel-density fits to correlation weighted distributions with a minimum correlation value of 0.5. The respective expected backazimuth (theo. Baz.) is indicated as a black, dashed line with a  $\pm 10^\circ$  interval in gray. For each frequency band  $i=1.0-5.0$  Hz,  $m=0.5-1.0$  Hz,  $a=0.1-0.5$  Hz and  $0.8-1.0$  Hz and each method Love (grid search based on Love wave polarization), Rayleigh (grid search based on Rayleigh wave polarization), Co.Var. (covariance optimization using horizontal rotation rates and seismic array beamforming (using vertical velocities). Standard deviations are displayed as vertical error bars.

cantly from the expected backazimuth. For the  $M_w$  6.2 event, all approaches yield directions in agreement with the expected backazimuth of 179 degrees for the dominant part of the surface waves (see Fig. 9). The CoVar approach yields the most stable estimates ( $CC > 0.9$ ), whereas backazimuth estimates for Love and Rayleigh polarization reveal more variance around the expected backazimuth for equally high CC values. For the wavefield coda, CC values decrease and directions scatter significantly around the expected backazimuth.

For each frequency band imposed by ADR a backazimuth estimation for different approaches is presented in Figures 10a and 10b for the  $M_w$  4.1 event and  $M_w$  6.2 event, respectively. The three 6 DoF approaches are applied using direct rotational observation and ADR. Established seismic array f-k beamforming for vertical components serves as a reference for backazimuth estimation. Mean backazimuth estimates and standard deviations are obtained from the peaks and variances of the kernel-density estimates, as shown in Figures 8 and 9.

#### 4.4 Seismic Phase Velocities

Observing 6 DoF of the seismic wavefield provides direct access to local seismic phase velocities of fundamental mode, plane-waves utilizing amplitude ratios for

1. Love waves:

$$c_{Love,phase} = -\frac{1}{2} \frac{a_T}{\Omega_z}, \quad (1)$$

2. Rayleigh waves:

$$c_{Rayleigh,phase} = \frac{a_z}{\Omega_T}, \quad (2)$$

with  $a$  denoting translation acceleration,  $\Omega$  rotation rate and  $T$  and  $z$  transverse and vertical components, respectively (e.g., Pancha et al., 2000; Igel et al., 2007, 2014; Kurrle et al., 2010). As for many detected events the entire waveform is compromised by self-noise and phase identification is difficult, we focus on peak amplitudes between 1 Hz and 20 Hz. Average apparent phase velocities are estimated for SH-polarized and

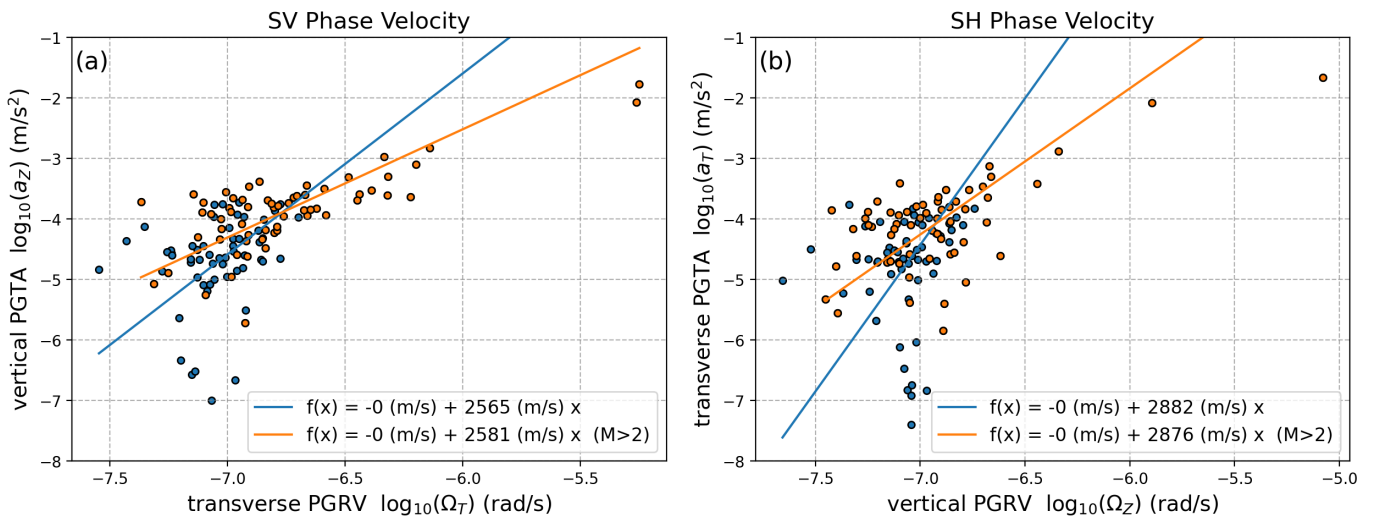


**Figure 11** Estimates of (a) SV-wave and (b) SH-wave phase velocities based on equations (1) and (2) using peak ground translation acceleration (PGTA) and peak ground rotation velocity (PGRV) amplitudes (instead of windows phase) for the subset with a coincidence trigger of six (118 events). An orthogonal distance regression is used to determine the phase velocity (= slope) for all events (blue and orange circles) and events with magnitude above two only (orange circles). Components are rotated to a ZRT system based on the theoretical backazimuth from catalog locations before peak amplitudes are picked.

SV-polarized waves using peak ground rotation velocity (PGRV) and peak ground translation acceleration (PGTA) amplitudes according to equations (1) and (2), respectively. Here, the assumptions on which equations (1) and (2) are based, could be called into question. Components are rotated to a ZRT system based on the expected backazimuth from catalog locations before peak amplitudes are determined. The velocity is estimated as the slope of an orthogonal distance regression by enforcing the intercept to equal zero. This approach yields an apparent phase velocity of about 2882 m/s for SH-polarized waves and about 2565 m/s for SV-polarized waves, using all 118 events (with a coincidence equal to 6). When only events with a magnitude above 2 are considered, apparent phase velocities of 2876 m/s and 2581 m/s for SH- and SV-polarized wave phase velocities are obtained, respectively (Fig. 11). Since no direct seismic phases are analyzed, the velocities are not linked to Rayleigh or Love waves directly and an uncertainty arising by using peak amplitudes and merely 118 events has to be taken into account. As the peak amplitudes of a broadband signal (1 Hz to 20 Hz) are linked to higher frequencies, these statistically estimated velocities sample the near-surface velocity structure. Fletcher et al. (1990) report shallow interval velocities for S-waves of about 3000 m/s (at 60 m to 300 m) overlaid by interval velocities of about 1600 m/s. The estimated average velocities shown in Figure 11 appear realistic.

In order to demonstrate the estimation of phase velocities for Rayleigh and Love waves, we analyze our two selected events. For moving time windows of 2 seconds and 50% overlap (before and after), we compute orthogonal distance regressions amplitude ratios according to equations (1) and (2) to estimate Love and Rayleigh phase velocities. Figure 12 shows waveforms and phase velocity estimates for the  $M_w$  4.1 and  $M_w$  6.2 events, color-coded by zero-lag CC values. Components are rotated to a ZRT system using the expected backaz-

imuth. Phase mismatches in waveforms that are projected into velocity estimates might result from differences in actual backazimuth due to scattering and the expected backazimuth of plane waves along a great circle path. An interpretation towards associated phase velocities has to assume distinct phases of plane Rayleigh and Love waves, which is challenging for local events of short duration, in particular for higher frequencies. For both exemplary events, we focus on the frequency band between 0.5 Hz to 1.0 Hz, with good rotational waveforms (see Figs. 6 and 5). The dispersive character of surface waves only allows obtaining average phase velocity estimates for this frequency band. The assumption of dominant fundamental mode surface waves has to be satisfied. For the  $M_w$  4.1 event, velocity estimates in this frequency band with high CC coefficients ( $>0.9$ ) range within 1500-2000 m/s and 2500-3500 m/s for Love and Rayleigh wave phase velocities, respectively (here the sample between 18 s and 19 s after the start of the trace with 4500 m/s is considered unreliable and neglected). For the  $M_w$  6.2 event, Rayleigh waves after 20 s show high CC values ( $>0.9$ ) and a phase velocity between 3500-4500 m/s (Fig. 12h). Love wave phase velocity estimates for time windows at 25 s after the start of the trace amount to 4000 m/s, whereas for time windows between 34 s and 45 s the range is 2000-3200 m/s (Fig. 12f).

## 5 Empirical Scaling Relation for Rotation Rates

In order to quantify the potential observations of a 6 DoF station with a blueSeis-3A sensor for studying the local and regional seismicity, we require a relation of magnitude and hypocentral distance with rotation rate amplitudes. Chow et al. (2019) used teleseismic observations to infer a logarithmic relation for vertical rotation rates (Love waves). We follow a similar approach to infer an empirical scaling relation based on a local magnitude

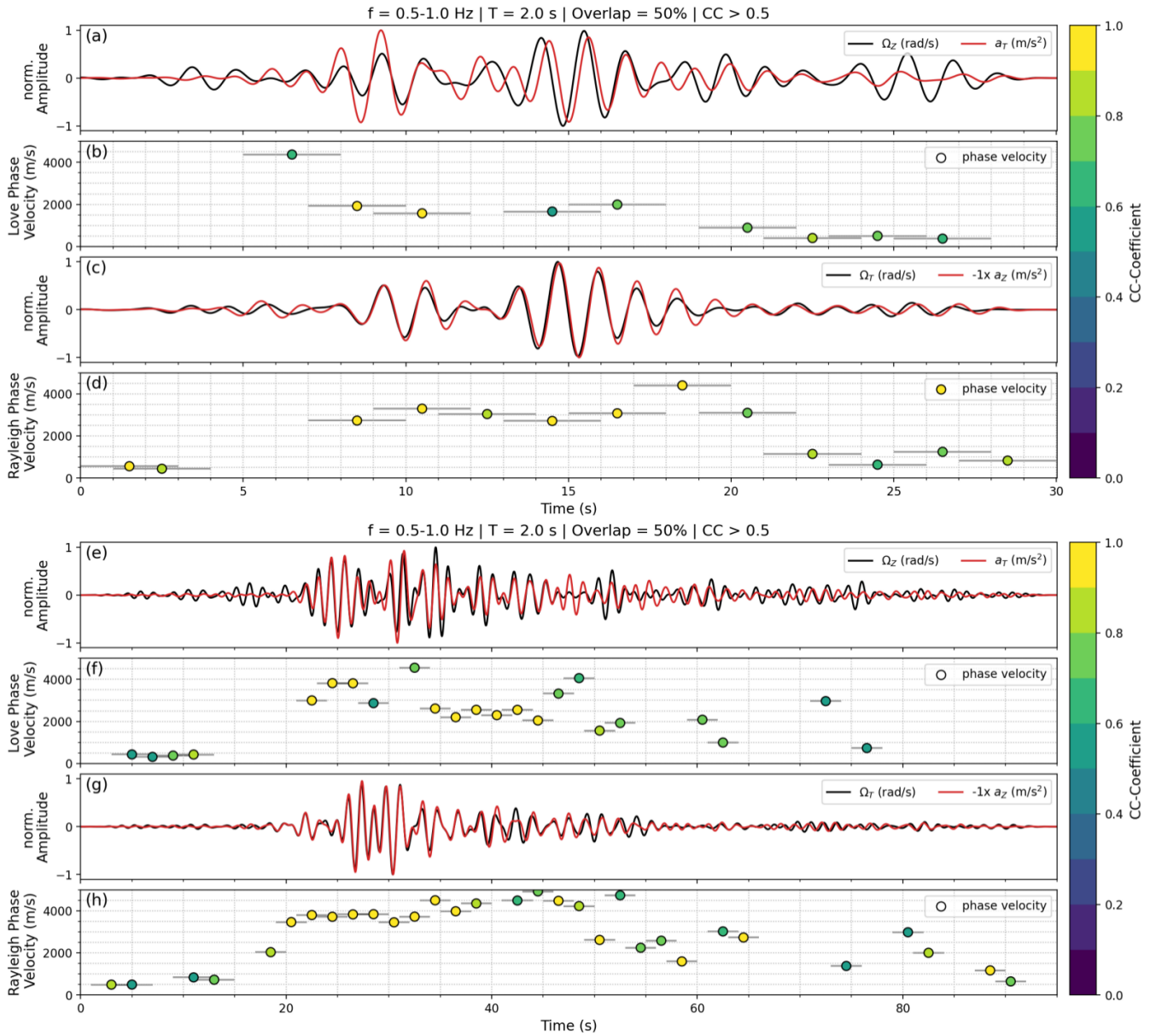


**Figure 12** Normalized waveforms and phase velocity estimates are shown in (a) to (d) for the  $M_w$  4.1 event and in (e) to (h) for the  $M_w$  6.2 event. (a) and (e) show component combinations for Love waves (vertical rotation rate  $\Omega_z$  and transverse acceleration  $a_T$ ), while (c) and (g) show combinations for Rayleigh waves (vertical acceleration  $a_Z$  and transverse rotation rate  $\Omega_r$ ). A bandpass filter is applied (0.5-1.0 Hz). Phase velocity estimates in 2 s time windows with 50% overlap (indicated by horizontal error bars) are based on amplitude ratios (Eq. (1) and Eq. (2)). Each velocity estimate is color-coded by the corresponding maximal, zero-lag cross-correlation (CC) coefficient of the waveforms in the time window.

scale for horizontal and vertical peak ground rotation rates individually:

$$M_L = \log_{10}(A_{max}) + a \log_{10}(R) + b R + c \quad (3)$$

with  $R$  being the hypocentral distance in km and  $A_{max}$  the peak ground rotation rate for horizontal PGRV:

$$A_{max} = \sqrt{A_N^2 + A_E^2},$$

and vertical PGRV

$$A_{max} = \sqrt{A_Z^2}.$$

For this purpose, we use a reduced dataset of 118 events triggered on all six components to pick peak

ground rotation rates in a frequency band of 1 Hz to 20 Hz (a sampling rate of 40 Hz imposes a limit for the first half year of data). This results in a linear system of equations of the form:

$$\begin{bmatrix} M_0 - \log_{10}(A_{max,0}) \\ \vdots \\ M_i - \log_{10}(A_{max,i}) \end{bmatrix} = \begin{pmatrix} \log_{10}(R_0) & R_0 & 1 \\ \vdots & \vdots & \vdots \\ \log_{10}(R_i) & R_i & 1 \end{pmatrix} \times \begin{bmatrix} a \\ b \\ c \end{bmatrix} \quad (4)$$

that allows to solve for the coefficients  $a$ ,  $b$  and  $c$  using a least-squares misfit criterion. Peak amplitudes for the detected regional  $M_w$  6.2 event were added manually to add a constraint for larger distances and higher magnitudes. Peak amplitudes of small-magnitude events with a poor signal-to-noise ratio are more compromised

	a	b	c	$\sigma_a^2$	$\sigma_b^2$	$\sigma_c^2$
$M_L$ (vertical)	1.42	0.00652	6.42	0.114	$1.88e^{-6}$	0.177
$M_L$ (horizontal)	1.37	0.00695	6.40	0.0690	$1.14e^{-6}$	0.107
deviation	3.5%	6.6%	0.3%			

**Table 3** Coefficients a, b and c for an empirical scaling relation for vertical and horizontal rotation velocities as defined in equation (3) and their variances ( $\sigma^2$ ) as obtained by a least-squares minimization.

by sensor self-noise. Therefore, events below  $M$  1 are down-weighted for the curve fit by assigning a higher variance of 5. High-magnitude events ( $> M$  2.5) are up-weighted instead using a lower variance value of 0.5, while all others are assigned a default variance value of 1. The coefficients for vertical and horizontal rotation rates of equation (3) and variance values are obtained using a least-squares optimization and listed in Table 3. Deviations between the final coefficients of vertical and horizontal rotation rates are as low as 0.3% for c and maximal for b with 6.6%. Variances listed in Table 3 are provided by the employed method *curve\_fit* of the SciPy python package (Virtanen et al., 2020).

Figure 13 visualizes the empirical scaling relations for a regional range of hypocentral distance up to 350 km and magnitudes up to  $M_w$  6.5. For a hypothetical  $M$  3.0 event at 50 km hypocentral distance, we would consequently expect vertical rotation rates of  $0.69 \mu\text{rad/s}$  and horizontal rotation rates of  $0.84 \mu\text{rad/s}$ . The shown self-noise limits for the blueSeis-3A sensor are extracted from operational range diagrams by Bernauer et al. (2018) and represent a minimum detection threshold at 10 nrad/s and 30 nrad/s for 1 Hz and 10 Hz, respectively (Fig. 13). A limit based on the rotational low noise model for transverse rotations by Brotzer et al. (2023) based on rms amplitudes of the model at 1 Hz provides a lowermost resolvable level (see Fig. 13). The shaded area for Figure 13 indicates a poor model resolution, thus no reliability in this magnitude-distance range due to missing observational constraints.

## 6 Discussion

### 6.1 Comparison of single-station and array-derived rotations

In the absence of portable rotational sensors, array-derived rotations served as a means to access rotational ground motions for 6 DoF waveform analysis (Spudich and Fletcher, 2008, 2009a). ADR also served as a benchmark for observations of large-scale ring laser gyroscopes (e.g., Suryanto et al., 2006; Donner et al., 2017). ADR, however, is based on assumptions such as plane-wave propagation and a rigid baseplate below the array stations, which hold best for low-frequency teleseismic events (Suryanto et al., 2006). When targeting regional or local seismicity, the higher frequencies dominate and a plane wave assumption will eventually not hold, for instance due to small-scale scattering effects. The inner PFO array allowed a comparison of direct observations and ADR estimates for frequencies up to 5 Hz, revealing strong variations in peak rotation rate amplitudes, while for lower frequencies, rotation rate am-

plitudes of direct observations and ADR are comparable, if the signal-to-noise ratio allows for a comparison. This gives confidence that both approaches are working. We observe generally lower peak amplitudes for ADR compared to direct observations of BSPF. Single-station ground rotation observations are very sensitive to local heterogeneities. The ADR estimate is dependent on the array geometry and density. The discrepancy for the 1 Hz to 5 Hz frequency band for the  $M_w$  4.1 event may be due to two missing stations in the inner array at that time, emphasizing the importance of station geometry and density for reliable ADR estimates. Moreover, the assumption of a homogenous, rigid plate below the array stations (Spudich and Fletcher, 2009b) may result in underestimated amplitudes. This has to be further investigated with high-sensitivity, direct rotational observations as reference. These findings are important in particular when comparing direct measurements of rotation (or strain) with array-derived rotations (or strain) in areas with expected local lateral heterogeneities. A fraction of the amplitude differences between ADR and direct observations might be attributed to strain-induced rotations (e.g., van Driel et al., 2012) caused by a very local site effect at the single-point 6-DoF station.

### 6.2 Six Degree-of-Freedom Analysis

Applications of 6 DoF analysis for teleseismic events, which provide clear phase separation, low frequencies signal content and ensure that a plane wave can be assumed, produce accurate results (e.g., Sollberger et al., 2020; Igel et al., 2007). Challenges arise for local seismicity since most seismic energy is contained in higher frequencies ( $> 10$  Hz). Higher frequencies are known to be affected by scattering of local heterogeneities, thus plane-wave assumptions might not be justified. Due to small epicentral distances of local events, thus short travel times, a clear separation of seismic phases is not to be expected. The signal-to-noise ratio is essential to obtain good results for the 6 DoF analysis techniques, however, it varies strongly for the events of this dataset depending on their epicentral distance, magnitude and presumably the radiation pattern (see examples in Fig. 3). We apply basic 6 DoF processing techniques, such as backazimuth estimation and local phase velocity estimation, for a local  $M_w$  4.1 event and a regional  $M_w$  6.2 event. We focus on a frequency range of 0.5-1.0 Hz, which reveals a good signal-to-noise ratio.

Hereby, three different approaches to estimate the backazimuth are compared, while for both events a ratio of horizontal rotation rate amplitudes (CoVar) yields the closest estimates to the expected backazimuth based on the catalog event location. Approaches

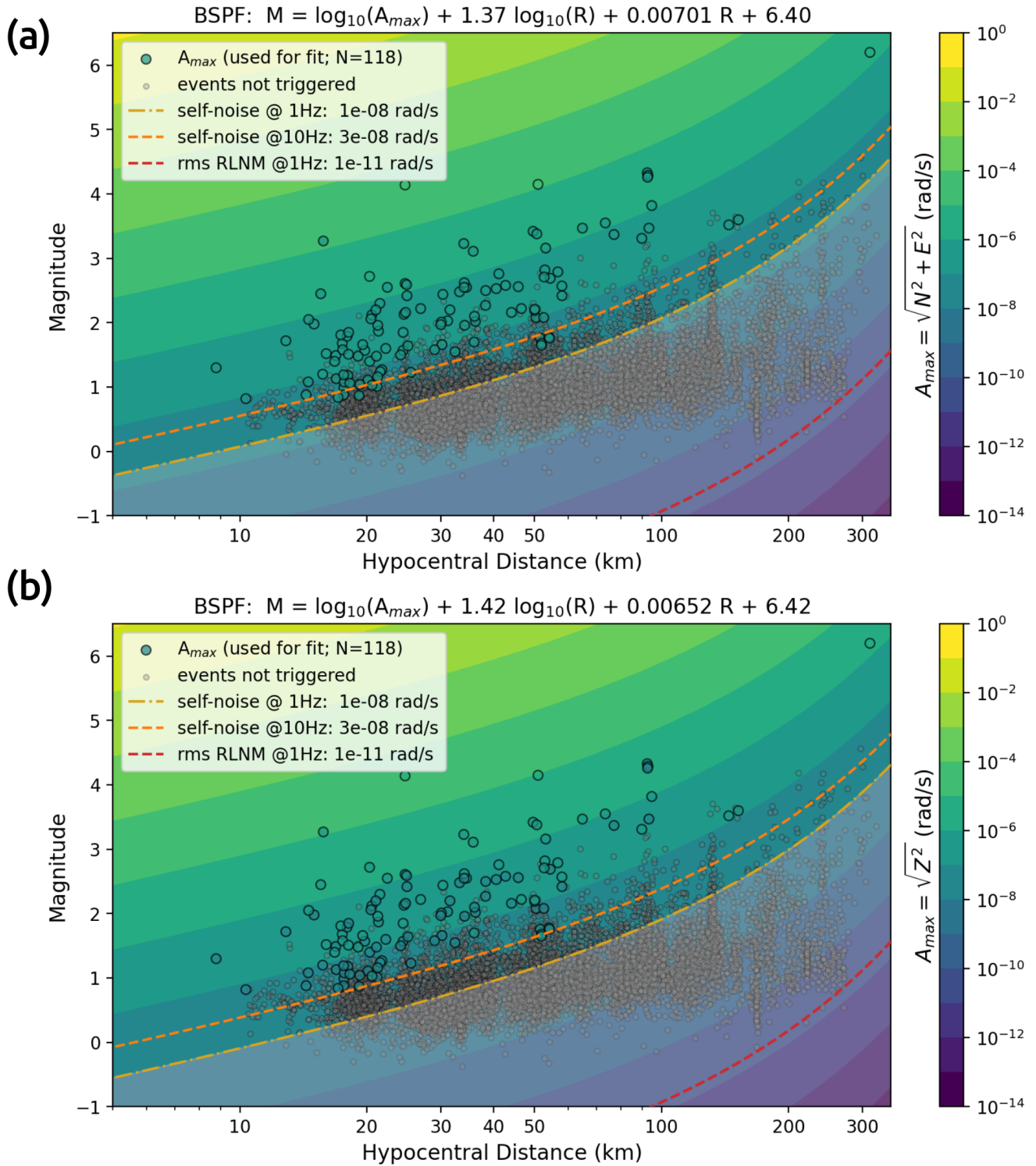


**Figure 13** This map shows the expected maximal (a) horizontal and (b) vertical rotation rates ( $A_{max}$ ) based on observations with a blueSeis-3A sensor at Piñon Flat Observatory. Color-coded circle represent observations of peak ground rotation velocities on all six channels (N=118) used for the determination of coefficients. Grey circles represent catalog events that are not triggered at the 6 DoF station. The self-noise level of the blueSeis-3A sensor is shown at 1 Hz ( $\approx 10$  nrad/s) and 10 Hz ( $\approx 30$  nrad/s), based on operational range diagrams by Bernauer et al. (2018). The rms amplitude value at 1 Hz of the rotational low noise model (RLNM) (Brotzer et al., 2023) is plotted as a lowermost value ( $\approx 10$  prad/s). The gray shaded area is poorly constrained, thus the model is not representative here.

based on Love and Rayleigh polarization require separated phases to exit adequate particle motion. For the local  $M_w$  4.1 event, array f-k beamforming is in good agreement with the expected backazimuth although the variance increases towards higher frequencies. The

backazimuth estimation for ADR and direct rotation observations show poor results with high variance for the  $i$ -band (1.0 Hz to 5.0 Hz). For the  $m$ -band (0.5 Hz to 1.0 Hz), the CoVar approach yields the best estimates for both events. The signal-to-noise ratio is poor for

the  $a$ -band, thus any interpretation not suitable. With regard to the  $i$ -band estimates for the  $M_w$  6.2 event, low accuracies and high variance is observed and also the beamforming reveals a strong offset compared to the expected backazimuth. Good signal-to-noise ratios in the  $a$ -band and  $m$ -band result in backazimuth estimates close to the expected backazimuth, except of the Rayleigh approach being far off the expected backazimuth.

Phase velocities for Love and Rayleigh waves are estimated for both events (Fig. 12). Near-surface shear-wave velocities of around 3000 m/s are reported from boreholes reaching depths of around 300 m (Fletcher et al., 1990). Vernon et al. (1998) report strong velocity heterogeneities close to the surface at the site of the PFO. The estimated Love wave phase velocity for the  $M_w$  4.1 event is lower than expected, with phase velocities of 1500-2000 m/s. This might be related to a violated assumption of dominantly fundamental mode surface waves. Later Love waves for the  $M_w$  6.2 event with reduced velocities (2000-3200 m/s; Fig. 12f) are likely related to scattered or converted waves linked to the heterogeneous near-surface wave guide at the site (Vernon et al., 1998). Scattering effects are also expected from the lateral variation in topography.

### 6.3 Empirical Scaling Relation for Rotation Rates

A first empirical amplitude relation map for vertical and horizontal rotation rates for local to regional scale seismicity is presented in Figures 13a and 13b and may serve as an orientation towards resolvability of seismic events for future campaigns with a comparable station setup. These empirical relations are derived using 118 events with a coincidence of 6. The applicability is likely restricted to the incorporated cluster of observed magnitudes and hypocentral distances and merely extrapolated outside. Apart from the  $M_w$  6.2 event, further constraints for regional distances and larger magnitudes are missing. We are aware that the transferability is not universal, and the relation is primarily valid for this station setup and location geology. In particular, settings with soft sediments likely amplify amplitudes, thus decreasing the resolution limit, despite the fixed self-noise level. Nevertheless, this serves well as a first orientation enabled by the long dataset of a permanent installation.

## 7 Conclusions

We report on a first permanent 6 DoF station, comprising a rotation rate sensor (blueSeis-3A gyroscope) and a broadband seismometer, at the Piñon Flat Observatory in southern California. Compared to the former one-component GEOSensor gyroscope (Schreiber et al., 2009), this station runs continuously with low maintenance effort. The data is openly accessible to the scientific community via IRIS FDSN services. Since it is located in a tectonically active area embedded in the well-instrumented Piñon Flat Observatory infrastructure and scientifically interesting area, we are sure it can contribute to further valuable observations and

studies. We evaluate a first dataset of the local to regional seismicity using one year of data from October 2022 to October 2023. The origin of most detected events is within an epicentral distance of 150 km from the station and cover a magnitude range from below 1.0 to 4.6, while not all events are detected on all six components. An exception is a regional  $M_w$  6.2 event with an epicentral distance of 312 km.

Direct rotational motion observations are compared to ADR in a frequency range from 0.1 Hz to 5.0 Hz using three subarrays of the PFO seismic array. CC values of above 0.9 indicate a good match in waveforms for lower frequency bands given a sufficient signal-to-noise ratio, as shown for a local  $M_w$  4.1 and a regional  $M_w$  6.2 event. For frequencies above 1 Hz, direct and ADR amplitudes differ significantly. Instead of an averaged rotational motion across an array of stations, a rotational sensor provides direct point observations of the curl of the seismic wavefield. A contribution to the discrepancy might be a result of strain-rotation coupling at local heterogeneities, which was not investigated further in this study.

The signal-to-noise ratio is essential to obtain good results for the 6 DoF analysis techniques, however, it varies strongly for the events of this dataset depending on their epicentral distance, magnitude and presumably the radiation pattern (see examples in Fig. 3). A comparison of ADR and PY.BSPF in terms of signal-to-noise ratio yields better results for ADR, profiting from low self-noise levels of seismometers. This comparison is, however, limited by the imposed frequency bands of the subarray geometry. Most signal energy for direct observations of PY.BSPF is generally found between 10 Hz and 30 Hz, therefore above of the range of the smallest array.

The 6 DoF analysis obtains good backazimuth estimates for all approaches, which are in agreement with the expected backazimuth. Estimated Rayleigh phase velocities of 3000-4000 m/s meet expectations for the site. Love wave phase velocities are partially lower than expected (2000-3000 m/s). Underlying assumptions of the approach, such as dominant fundamental modes and plane waves, have to be fulfilled, thus local heterogeneities have to be considered. With more high quality events, local heterogeneities can also be studied using 6 DoF methodology. Furthermore, we used peak rotation rate observations of 118 events to infer an empirical amplitude relation for peak vertical and horizontal rotation rates based on a local magnitude scale equation. Determined coefficients for this empirical amplitude relation for vertical and horizontal rotation rates are very similar (0.3% - 6.6% deviation). Validity of the empirical relations below the self-noise level is not guaranteed, therefore shaded. The presented relations might serve as orientation for further installations of 6 DoF, especially for this type of sensor, in order to study local and regional seismicity.

We find that the current limitation for observations is set by the self-noise limit of the blueSeis-3A sensor. In order to complete observations at lower-magnitudes for local seismicity or mid-magnitudes for regional seismicity, the self-noise limit has to be decreased by about

3 to 4 orders of magnitude (see Fig. 13; Brotzer et al. (2023)). This is especially required for studies based on ambient seismic noise sources, such as seismic microseism (Hadziioannou et al., 2012), which are at the moment deeply hidden in the self-noise of this sensor.

## Acknowledgements

Andreas Brotzer is grateful for being awarded the Jerome M. Paros Scholarship by the American Geophysical Union in 2021 enabling his research stay at the Scripps Institution of Oceanography in San Diego in 2022 under supervision of Mark Zumberge. This stay included the deployment of the blueSeis-3A at the Piñon Flat Observatory. Heiner Igel thanks the Cecil and Ida Green Foundation for the Fellowship in 2022 and 2023. Our gratitude goes to the staff at Scripps, namely Sonya Wilson, William Hatfield and Daniel Auerbach, who helped with the logistics and setup of the sensor at PFO. We would also like to thank the EarthScope Consortium, formerly Incorporated Research Institutions for Seismology (IRIS), for providing the blueSeis-3A sensor for this deployment. We appreciate the research funding and support of the faculty of geosciences of the Ludwig-Maximilians-Universität München, Germany. Computing resources are funded by the Deutsche Forschungsgemeinschaft (DFG, German Research Foundation) – 518204048. We also want to thank Tobias Megies for incorporating the BSPF station into the rotational database. We acknowledge the time invested and appreciate the thoughtful suggestions provided by the reviewers of this article, namely Stefanie Donner and Oliver Lamb.

## Data and code availability

Processed data, metadata not available online as well as Jupyter notebooks and python scripts to create the shown figures are provided at these repositories:

- <https://github.com/andbrocode/BlueSeisPinonFlat>
- <https://doi.org/10.5281/zenodo.11582084>
- <https://syncandshare.lrz.de/getlink/fixXq8RsYcpwAzLa7hZ4YbT/Seismica-PFO-BlueSeis-2024>

## Competing interests

The authors have no competing interests.

## References

- Abreu, R., Durand, S., Rost, S., and Thomas, C. Deep Earth rotational seismology. *Geophysical Journal International*, 234(3): 2365–2374, Sept. 2023. doi: 10.1093/gji/ggad245.
- Agnew, D. C. and Wyatt, F. K. Long-Base Laser Strainmeters: A Review. Jan. 2003. <https://escholarship.org/uc/item/21z72167>.
- Aki, K. and Richards, P. G. *Quantitative Seismology, 2nd Ed.* 2002.
- Belfi, J., Beverini, N., Bosi, F., Carelli, G., Cuccato, D., De Luca, G., Di Virgilio, A., Gebauer, A., Maccioni, E., Ortolan, A., Porzio, A., Saccorotti, G., Simonelli, A., and Terreni, G. Deep underground rotation measurements: GINGERino ring laser gyroscope in Gran Sasso. *Review of Scientific Instruments*, 88(3): 034502, Mar. 2017. doi: 10.1063/1.4977051.
- Bernauer, F., Wassermann, J., and Igel, H. Rotational sensors—A comparison of different sensor types. *Journal of seismology*, 16: 595–602, 2012. doi: 10.1007/s10950-012-9298-3.
- Bernauer, F., Wassermann, J., Guattari, F., Frenois, A., Bigueur, A., Gaillot, A., de Toldi, E., Ponceau, D., Schreiber, U., and Igel, H. BlueSeis3A: Full characterization of a 3C broadband rotational seismometer. *Seismological Research Letters*, 89(2A):620–629, 2018. doi: 10.1785/0220170143.
- Bernauer, F., Wassermann, J., and Igel, H. Dynamic tilt correction using direct rotational motion measurements. *Seismological Research Letters*, 91(5):2872–2880, 2020. doi: 10.1785/0220200132.
- Bernauer, F., Behnen, K., Wassermann, J., Egdorf, S., Igel, H., Donner, S., Stammler, K., Hoffmann, M., Edme, P., Sollberger, D., Schmelzbach, C., Robertsson, J., Paitz, P., Igel, J., Smolinski, K., Fichtner, A., Rossi, Y., Izgi, G., Vollmer, D., Eibl, E. P. S., Buske, S., Veress, C., Guattari, F., Laudat, T., Mattio, L., Sèbe, O., Olivier, S., Lallemand, C., Brunner, B., Kurzych, A. T., Dudek, M., Jaroszewicz, L. R., Kowalski, J. K., Bońkowski, P. A., Bobra, P., Zembaty, Z., Vackář, J., Málek, J., and Brokesova, J. Rotation, Strain, and Translation Sensors Performance Tests with Active Seismic Sources. *Sensors*, 21(1):264, Jan. 2021. doi: 10.3390/s21010264.
- Beyreuther, M., Barsch, R., Krischer, L., Megies, T., Behr, Y., and Wassermann, J. ObsPy: A Python toolbox for seismology. *Seismological Research Letters*, 81(3):530–533, 2010. doi: 10.1785/gssrl.81.3.530.
- Bońkowski, P., Bobra, P., Zembaty, Z., and Jędraszak, B. Experimental Analysis of Stiffness Identification of Damaged Reinforced Concrete Beams with Directly Measured Rotational Modes (preprint). 2023. doi: 10.2139/ssrn.4552257.
- Brotzer, A., Igel, H., Stutzmann, E., Montagner, J., Bernauer, F., Wassermann, J., Widmer-Schmidrig, R., Lin, C., Kiselev, S., Vernon, F., and Schreiber, K. U. Characterizing the Background Noise Level of Rotational Ground Motions on Earth. *Seismological Research Letters*, Dec. 2023. doi: 10.1785/0220230202.
- Chen, C., Wang, Y., Sun, L., Lin, C., Wei, Y., Liao, C., Lin, B., and Qin, L. Six-Component Earthquake Synchronous Observations Across Taiwan Strait: Phase Velocity and Source Location. *Earth and Space Science*, 10(12), Dec. 2023. doi: 10.1029/2023ea003040.
- Chow, B., Wassermann, J., Schuberth, B. S. A., Hadziioannou, C., Donner, S., and Igel, H. Love wave amplitude decay from rotational ground motions. *Geophysical Journal International*, 218(2):1336–1347, Aug. 2019. doi: 10.1093/gji/ggz213.
- Cochard, A., Igel, H., Schuberth, B., Suryanto, W., Velikoseltsev, A., Schreiber, U., Wassermann, J., Scherbaum, F., and Vollmer, D. Rotational Motions in Seismology: Theory, Observation, Simulation. In Teisseyre, R., Majewski, E., and Takeo, M., editors, *Earthquake Source Asymmetry, Structural Media and Rotation Effects*, pages 391–411. Springer-Verlag, Berlin/Heidelberg, 2006. doi: 10.1007/3-540-31337-0\_30.
- Dataset., S. C. E. C. C. 2013. doi: 10.7909/C3WD3xH1.
- Donner, S. *Rotational ground motion measurements for regional seismic moment tensors: A review*, pages 141–186. Elsevier, 2021. doi: 10.1016/bs.agph.2021.06.002.
- Donner, S., Bernauer, M., and Igel, H. Inversion for seismic moment tensors combining translational and rotational ground motions. *Geophysical Journal International*, 207:562 – 570, 2016. doi: 10.1093/gji/ggw298.
- Donner, S., Lin, C., Hadziioannou, C., Gebauer, A., Vernon, F., Ag-

- new, D. C., Igel, H., Schreiber, U., and Wassermann, J. Comparing Direct Observation of Strain, Rotation, and Displacement with Array Estimates at Piñon Flat Observatory, California. *Seismological Research Letters*, 88(4):1107–1116, 05 2017. doi: 10.1785/0220160216.
- Donner, S., Igel, H., Hadziioannou, C., and the Romy group. Retrieval of the Seismic Moment Tensor from Joint Measurements of Translational and Rotational Ground Motions: Sparse Networks and Single Stations. In *Moment Tensor Solutions*, pages 263–280. Springer International Publishing, 2018. doi: 10.1007/978-3-319-77359-9\_12.
- Donner, S., Mustač, M., Hejrani, B., Tkalčić, H., and Igel, H. Seismic moment tensors from synthetic rotational and translational ground motion: Green's functions in 1-D versus 3-D. *Geophysical Journal International*, 223(1):161–179, jun 2020. doi: 10.1093/gji/ggaa305.
- Eibl, E. P., Roskopf, M., Sciotto, M., Currenti, G., Di Grazia, G., Jousset, P., Krüger, F., and Weber, M. Performance of a rotational sensor to decipher volcano seismic signals on Etna, Italy. *Journal of Geophysical Research: Solid Earth*, 127(6):e2021JB023617, 2022. doi: 10.1029/2021JB023617.
- Fletcher, J. B., Fumal, T., Liu, H.-P., and Carroll, L. C. Near-surface velocities and attenuation at two boreholes near Anza, California, from logging data. *Bulletin of the Seismological Society of America*, 80(4):807–831, 1990. doi: 10.1785/BSSA0800040807.
- Guéguen, P. and Astorga, A. The Torsional Response of Civil Engineering Structures during Earthquake from an Observational Point of View. *Sensors*, 21(2):342, jan 2021. doi: 10.3390/s21020342.
- Guéguen, P., Guattari, F., Aubert, C., and Laudat, T. Comparing Direct Observation of Torsion with Array-Derived Rotation in Civil Engineering Structures. *Sensors*, 21(1):142, dec 2020. doi: 10.3390/s21010142.
- Hadziioannou, C., Gaebler, P., Schreiber, U., Wassermann, J., and Igel, H. Examining ambient noise using colocated measurements of rotational and translational motion. *Journal of Seismology*, 16(4):787–796, Oct. 2012. doi: 10.1007/s10950-012-9288-5.
- Ichinose, G. A., Ford, S. R., and Mellors, R. J. Regional Moment Tensor Inversion Using Rotational Observations. *Journal of Geophysical Research: Solid Earth*, 126(2):e2020JB020827, 2021. doi: 10.1029/2020JB020827.
- Igel, H., Schreiber, U., Flaws, A., Schubert, B., Velikoseltsev, A., and Cochard, A. Rotational motions induced by the M8. 1 Tokachi-oki earthquake, September 25, 2003. *Geophysical research letters*, 32(8), 2005. doi: 10.1029/2004GL022336.
- Igel, H., Cochard, A., Wassermann, J., Flaws, A., Schreiber, U., Velikoseltsev, A., and Pham Dinh, N. Broad-band observations of earthquake-induced rotational ground motions. *Geophysical Journal International*, 168(1):182–196, Jan. 2007. doi: 10.1111/j.1365-246X.2006.03146.x.
- Igel, H., Bernauer, M., Wassermann, J., and Schreiber, K. U. Seismology, Rotational, Complexity. In Meyers, R. A., editor, *Encyclopedia of Complexity and Systems Science*, pages 1–26. Springer, Berlin, Heidelberg, 2014. doi: 10.1007/978-3-642-27737-5\_608-1.
- Igel, H., Schreiber, K. U., Gebauer, A., Bernauer, F., Egdorf, S., Simonelli, A., Lin, C.-J., Wassermann, J., Donner, S., Hadziioannou, C., Yuan, S., Brotzer, A., Kodet, J., Tanimoto, T., Hugentobler, U., and Wells, J.-P. R. ROMY: a multicomponent ring laser for geodesy and geophysics. *Geophysical Journal International*, 225(1):684–698, 01 2021. doi: 10.1093/gji/ggaa614.
- Keil, S., Wassermann, J., and Igel, H. Single-station seismic microzonation using 6C measurements. *Journal of Seismology*, 25(1): 103–114, 2021. doi: 10.1007/s10950-020-09944-1.
- Kurrle, D., Igel, H., Ferreira, A., Wassermann, J., and Schreiber, K. Can we estimate local Love wave dispersion properties from collocated amplitude measurements of translations and rotations? *Geophysical Research Letters*, 37, 02 2010. doi: 10.1029/2009GL042215.
- Lin, C.-J., Ku, C.-S., Chi, T.-C., Huang, B.-S., Huang, H.-H., and Liu, C.-C. Correcting the Background Tilt Signal of the Horizontal Seismometer Using a Rotation Sensor. *Seismological Research Letters*, 93(3):1564–1572, mar 2022. doi: 10.1785/0220210185.
- Lindner, F., Wassermann, J., Schmidt-Aursch, M. C., Schreiber, K. U., and Igel, H. Seafloor Ground Rotation Observations: Potential for Improving Signal-to-Noise Ratio on Horizontal OBS Components. *Seismological Research Letters*, 88(1):32–38, Nov. 2016. doi: 10.1785/0220160051.
- McCann, J. J., Winterflood, J., Ju, L., and Zhao, C. A multi-orientation low-frequency rotational accelerometer. *Review of Scientific Instruments*, 92(6):064503, jun 2021. doi: 10.1063/5.0047069.
- Pancha, A., Webb, T. H., Stedman, G. E., McLeod, D. P., and Schreiber, K. U. Ring laser detection of rotations from teleseismic waves. *Geophysical Research Letters*, 27(21):3553–3556, 2000. doi: 10.1029/2000GL011734.
- Perron, V., Hollender, F., Mariscal, A., Theodoulidis, N., Andreou, C., Bard, P., Cornou, C., Cottureau, R., Cushing, E. M., Frau, A., Hok, S., Konidakis, A., Langlaude, P., Laurendeau, A., Savvaidis, A., and Svay, A. Accelerometer, Velocimeter Dense-Array, and Rotation Sensor Datasets from the Sinaps@ Post-seismic Survey (Cephalonia 2014–2015 Aftershock Sequence). *Seismological Research Letters*, 89(2A):678–687, Mar. 2018. doi: 10.1785/0220170125.
- Poppeliers, C. and Evans, E. V. The effects of measurement uncertainties in seismic-wave gradiometry. *Bulletin of the Seismological Society of America*, 105(6):3143–3155, 2015. doi: 10.1785/0120150043.
- Ross, M. P., Venkateswara, K., Hagedorn, C. A., Gundlach, J. H., Kissel, J. S., Warner, J., Radkins, H., Shaffer, T. J., Coughlin, M. W., and Bodin, P. Low-Frequency Tilt Seismology with a Precision Ground-Rotation Sensor. *Seismological Research Letters*, 89(1):67–76, nov 2017a. doi: 10.1785/0220170148.
- Ross, M. P., van Dongen, J., Huang, Y., Zhou, H., Chowdhury, Y., Apple, S. K., Mow-Lowry, C. M., Mitchell, A. L., Holland, N. A., Lantz, B., Bonilla, E., Engl, A., Pele, A., Griffith, D., Sanchez, E., Shaw, E. A., Gettings, C., and Gundlach, J. A vacuum-compatible cylindrical inertial rotation sensor with picoradian sensitivity. *Review of Scientific Instruments*, 94(9), Sept. 2023. doi: 10.1063/5.0167283.
- Ross, Z. E., Hauksson, E., and Ben-Zion, Y. Abundant off-fault seismicity and orthogonal structures in the San Jacinto fault zone. *Science advances*, 3(3):e1601946, 2017b. doi: 10.1126/sciadv.1601946.
- Salvermoser, J., Hadziioannou, C., Hable, S., Krischer, L., Chow, B., Ramos, C., Wassermann, J., Schreiber, U., Gebauer, A., and Igel, H. An Event Database for Rotational Seismology. *Seismological Research Letters*, 88(3):935–941, may 2017. doi: 10.1785/0220160184.
- Sbaa, S., Hollender, F., Perron, V., Imtiaz, A., Bard, P.-Y., Mariscal, A., Cochard, A., and Dujardin, A. Analysis of rotation sensor data from the SINAPS@ Kefalonia (Greece) post-seismic experiment—link to surface geology and wavefield characteristics. *Earth, Planets and Space*, 69(1):124, Sept. 2017. doi: 10.1186/s40623-017-0711-6.
- Schmelzbach, C., Donner, S., Igel, H., Sollberger, D., Taufiqurrahman, T., Bernauer, F., Häusler, M., Van Renterghem, C., Wasser-

- mann, J., and Robertsson, J. Advances in 6C seismology: Applications of combined translational and rotational motion measurements in global and exploration seismology. *GEOPHYSICS*, 83(3):WC53–WC69, May 2018. doi: 10.1190/geo2017-0492.1.
- Schreiber, K. U., Hautmann, J. N., Velikoseltsev, A., Wassermann, J., Igel, H., Otero, J., Vernon, F., and Wells, J.-P. R. Ring Laser Measurements of Ground Rotations for Seismology. *Bulletin of the Seismological Society of America*, 99(2B):1190–1198, May 2009. doi: 10.1785/0120080171.
- Schreiber, K. U., Gebauer, A., Igel, H., Wassermann, J., Hurst, R. B., and Wells, J.-P. R. The centennial of the Sagnac experiment in the optical regime: From a tabletop experiment to the variation of the Earth's rotation. *Comptes Rendus. Physique*, 15(10): 859–865, Oct. 2014. doi: 10.1016/j.crhy.2014.10.003.
- Singh, S., Capdeville, Y., and Igel, H. Correcting wavefield gradients for the effects of local small-scale heterogeneities. *Geophysical Journal International*, 220(2):996–1011, 2020. doi: 10.1093/gji/ggz479.
- Sollberger, D. solldavid/TwistPy: TwistPy - First release. July 2023. doi: 10.5281/zenodo.8124030.
- Sollberger, D., Greenhalgh, S. A., Schmelzbach, C., Van Renterghem, C., and Robertsson, J. O. 6-C polarization analysis using point measurements of translational and rotational ground-motion: theory and applications. *Geophysical Journal International*, 213(1):77–97, 2018. doi: 10.3390/s20236904.
- Sollberger, D., Igel, H., Schmelzbach, C., Edme, P., Van Manen, D.-J., Bernauer, F., Yuan, S., Wassermann, J., Schreiber, U., and Robertsson, J. O. A. Seismological Processing of Six Degree-of-Freedom Ground-Motion Data. *Sensors*, 20(23):6904, Dec. 2020. doi: 10.3390/s20236904.
- Sollberger, D., Heimann, S., Bernauer, F., Eibl, E. P., Donner, S., Hadziioannou, C., Igel, H., Yuan, S., and Wassermann, J. TwistPy: An open-source Python toolbox for wavefield inertial sensing techniques. In *EGU General Assembly Conference Abstracts*, pages EGU–7563, 2023. doi: 10.5194/egusphere-egu23-7563.
- Spudich, P. and Fletcher, J. B. Observation and prediction of dynamic ground strains, tilts, and torsions caused by the Mw6.0 2004 Parkfield, California, earthquake and aftershocks, derived from UPSAR array observations. *Bulletin of the Seismological Society of America*, 98(4):1898–1914, 2008. doi: 10.1785/0120070157.
- Spudich, P. and Fletcher, J. B. Software for inference of dynamic ground strains and rotations and their errors from short baseline array observations of ground motions. *Bulletin of the Seismological Society of America*, 99(2B):1480–1482, 2009a. doi: 10.1785/0120080230.
- Spudich, P. and Fletcher, J. B. Software for Inference of Dynamic Ground Strains and Rotations and Their Errors from Short Baseline Array Observations of Ground Motions. *Bulletin of the Seismological Society of America*, 99(2B):1480–1482, May 2009b. doi: 10.1785/0120080230.
- Suryanto, W., Igel, H., Wassermann, J., Cochard, A., Schuberth, B., Vollmer, D., Scherbaum, F., Schreiber, U., and Velikoseltsev, A. First comparison of array-derived rotational ground motions with direct ring laser measurements. *Bulletin of the Seismological Society of America*, 96(6):2059–2071, 2006. doi: 10.1785/0120060004.
- Takeo, M. Rotational Motions Observed during an Earthquake Swarm in April 1998 Offshore Ito, Japan. *Bulletin of the Seismological Society of America*, 99(2B):1457–1467, May 2009. doi: 10.1785/0120080173.
- Trifunac, M. D. The role of strong motion rotations in the response of structures near earthquake faults. *Soil Dynamics and Earthquake Engineering*, 29(2):382–393, feb 2009. doi: 10.1016/j.soildyn.2008.04.001.
- UC San Diego. Piñon Flats Observatory Array. 2014. doi: 10.7914/sn/py.
- van Driel, M., Wassermann, J., Nader, M. F., Schuberth, B. S. A., and Igel, H. Strain rotation coupling and its implications on the measurement of rotational ground motions. *Journal of Seismology*, 16(4):657–668, Oct. 2012. doi: 10.1007/s10950-012-9296-5.
- Venkateswara, K., Hagedorn, C. A., Gundlach, J. H., Kissel, J., Warner, J., Radkins, H., Shaffer, T., Lantz, B., Mittleman, R., Matichard, F., and Schofield, R. Subtracting Tilt from a Horizontal Seismometer Using a Ground-Rotation Sensor. *Bulletin of the Seismological Society of America*, pages 709–717, 2017. doi: 10.1785/0120160310.
- Vernon, F. L., Pavlis, G. L., Owens, T. J., McNamara, D. E., and Anderson, P. N. Near-surface scattering effects observed with a high-frequency phased array at Pinyon Flats, California. *Bulletin of the Seismological Society of America*, 88(6):1548–1560, 12 1998. doi: 10.1785/BSSA0880061548.
- Virtanen, P., Gommers, R., Oliphant, T. E., Haberland, M., Reddy, T., Cournapeau, D., Burovski, E., Peterson, P., Weckesser, W., Bright, J., van der Walt, S. J., Brett, M., Wilson, J., Millman, K. J., Mayorov, N., Nelson, A. R. J., Jones, E., Kern, R., Larson, E., Carey, C. J., Polat, İ., Feng, Y., Moore, E. W., VanderPlas, J., Laxalde, D., Perktold, J., Cimrman, R., Henriksen, I., Quintero, E. A., Harris, C. R., Archibald, A. M., Ribeiro, A. H., Pedregosa, F., van Mulbregt, P., and SciPy 1.0 Contributors. SciPy 1.0: Fundamental Algorithms for Scientific Computing in Python. *Nature Methods*, 17:261–272, 2020. doi: 10.1038/s41592-019-0686-2.
- Wassermann, J., Bernauer, F., Shiro, B., Johanson, I., Guattari, F., and Igel, H. Six-Axis Ground Motion Measurements of Caldera Collapse at Kilauea Volcano, Hawai'i—More Data, More Puzzles? *Geophysical Research Letters*, 47(5), 2020. doi: 10.1029/2019GL085999.
- Yuan, S., Simonelli, A., Lin, C.-J., Bernauer, F., Donner, S., Braun, T., Wassermann, J., and Igel, H. Six degree-of-freedom broadband ground-motion observations with portable sensors: Validation, local earthquakes, and signal processing. *Bulletin of the Seismological Society of America*, 110(3):953–969, 2020. doi: 10.1785/0120190277.
- Zembaty, Z., Kokot, S., and Bobra, P. Application of rotation rate sensors in measuring beam flexure and structural health monitoring. *Seismic Behaviour and Design of Irregular and Complex Civil Structures II*, pages 65–76, 2016. doi: 10.1007/978-3-319-14246-3\_6.

The article *On single-station, six degree-of-freedom observations of local to regional seismicity at the Piñon Flat Observatory in Southern California* © 2025 by Andreas Brotzer is licensed under CC BY 4.0.